Title

Single-Cell Profiling Reveals Divergent, Globally Patterned Immune Responses in Murine Skin Inflammation

Journal

iScience, 23(10)

ISSN

2589-0042

Authors

Liu, Yale
Cook, Christopher
Sedgewick, Andrew J
et al.

Publication Date

2020-10-01

DOI

10.1016/j.isci.2020.101582

iScience

CellPress
OPEN ACCESS

Article

Single-Cell Profiling Reveals Divergent, Globally Patterned Immune Responses in Murine Skin Inflammation

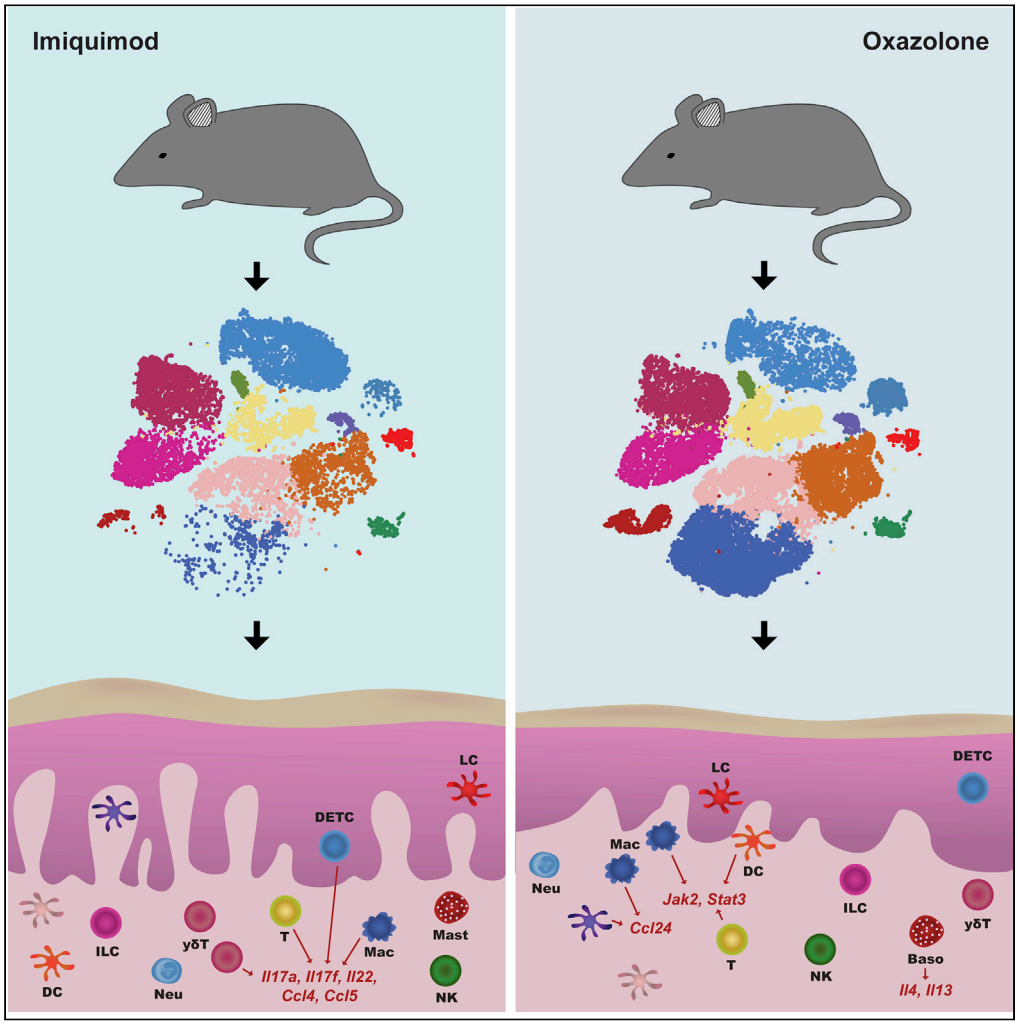

Yale Liu, Christopher Cook, Andrew J. Sedgewick, ..., Jun S. Song, Raymond J. Cho, Jeffrey B. Cheng

raymond.cho@ucsf.edu (R.J.C.)
jeffrey.cheng@ucsf.edu (J.B.C.)

HIGHLIGHTS

Oxazolone pervasively upregulates *Jak2/Stat3* expression across T cells and APCs

Il4/Il13 induction in skin by oxazolone is dominated by infiltrating basophils

Imiquimod broadly increases *Il17/Il22* and *Ccl4/Ccl5*, extending to non-T cells

Oxazolone induces more highly compartmentalized immune cell responses than imiquimod

Liu et al., iScience *23*, 101582
October 23, 2020
https://doi.org/10.1016/j.isci.2020.101582

iScience

CellPress
OPEN ACCESS

Article

Single-Cell Profiling Reveals Divergent, Globally Patterned Immune Responses in Murine Skin Inflammation

Yale Liu,[1,2,3,13] Christopher Cook,[1,2,13] Andrew J. Sedgewick,[4,13] Shuyi Zhang,[5] Marlys S. Fassett,[1,6] Roberto R. Ricardo-Gonzalez,[1,6] Paymann Harirchian,[1,2] Sakeen W. Kashem,[1] Sho Hanakawa,[7] Jacob R. Leistico,[5] Jeffrey P. North,[1] Mark A. Taylor,[1] Wei Zhang,[2] Mao-Qiang Man,[2] Alexandra Charruyer,[1,2] Nadejda Beliakova-Bethell,[8,12] Stephen C. Benz,[4] Ruby Ghadially,[2] Theodora M. Mauro,[2] Daniel H. Kaplan,[9] Kenji Kabashima,[7,10] Jaehyuk Choi,[11] Jun S. Song,[5] Raymond J. Cho,[1,14,*] and Jeffrey B. Cheng[1,2,14,15,*]

SUMMARY

Inflammatory response heterogeneity has impeded high-resolution dissection of diverse immune cell populations during activation. We characterize mouse cutaneous immune cells by single-cell RNA sequencing, after inducing inflammation using imiquimod and oxazolone dermatitis models. We identify 13 CD45$^+$ subpopulations, which broadly represent most functionally characterized immune cell types. Oxazolone pervasively upregulates *Jak2/Stat3* expression across T cells and antigen-presenting cells (APCs). Oxazolone also induces *Il4/Il13* expression in newly infiltrating basophils, and *Il4ra* and *Ccl24*, most prominently in APCs. In contrast, imiquimod broadly upregulates *Il17/Il22* and *Ccl4/Ccl5*. A comparative analysis of single-cell inflammatory transcriptional responses reveals that APC response to oxazolone is tightly restricted by cell identity, whereas imiquimod enforces shared programs on multiple APC populations in parallel. These global molecular patterns not only contrast immune responses on a systems level but also suggest that the mechanisms of new sources of inflammation can eventually be deduced by comparison to known signatures.

INTRODUCTION

The term "inflammation" serves as an abstraction that summarizes the activity of dozens of types of immune cells, whose global reprogramming by exogenous antigens counteracts pathologic intrusions. Until recently, the heterogeneity of the immune response has been addressed by applying flow cytometry and immunohistochemistry to interrogate specific subpopulations such as innate lymphoid cells (Sonnenberg and Artis, 2015), regulatory B cells (Rosser and Mauri, 2015), and regulatory T cells (Malhotra et al., 2018). Although these studies assigned functional repertoires to cellular subtypes, their scope limited systematic comparisons between cell types and the discovery of rare, functionally active cell subpopulations. The recent emergence of single-cell sequencing approaches has enabled the characterization of multiple, divergent immune cell populations in parallel (Villani et al., 2017).

Active inflammation typifies the skin, both in host defense and pathogenic processes that cause rashes. Studies using single-cell RNA-sequencing (scRNA-seq) have recently refined the contributions of T cells (Hughes et al., 2019), myeloid cell subsets (Jordão et al., 2019), keratinocytes (Cheng et al., 2018), and fibroblasts (Croft et al., 2019) to cutaneous inflammation. Because the skin is persistently, naturally exposed to exogenous provocation, it offers a tractable means to recapitulate physiologic inflammation. Indeed, mouse skin has been used to model common human rashes, using topical and systemic administration of inflammation-inducing agents. For example, application of oxazolone to mouse skin activates cytotoxic CD8$^+$ T cell-mediated delayed hypersensitivity, in which mast cells and neutrophils play a critical role in priming the inflammatory reaction (Dudeck et al., 2011; Vocanson et al., 2009; Weber et al., 2015). Oxazolone-mediated inflammation also appears to involve various dendritic and T helper (Th) cell types, the roles of which remain incompletely understood (Vocanson et al., 2009). In contrast, imiquimod, an agonist of Toll-like receptor 7, activates the IL-23/IL-17/IL-22-axis and interferon signaling pathways,

[1]Department of Dermatology, University of California, San Francisco, San Francisco, CA, USA

[2]Dermatology Service, San Francisco Veterans Administration Health Care System, San Francisco, CA, USA

[3]Department of Dermatology, the Second Affiliated Hospital of Xi'an Jiaotong University, ShaanXi, China

[4]ImmunityBio Inc, Culver City, CA, USA

[5]Department of Physics, Carl R. Woese Institute for Genomic Biology, University of Illinois at Urbana-Champaign, Champaign, IL, USA

[6]Department of Immunology and Microbiology, University of California, San Francisco, San Francisco, CA, USA

[7]Department of Dermatology, Kyoto University Graduate School of Medicine, Kyoto, Japan

[8]Department of Medicine, University of California San Diego, La Jolla, CA 92093-0679, USA

[9]Departments of Dermatology and Immunology, University of Pittsburgh, Pittsburgh, PA, USA

[10]Singapore Immunology Network (SIgN) and Skin Research Institute of Singapore (SRIS), Agency for Science, Technology and Research (A*STAR), Singapore, Singapore

[11]Department of Dermatology, Northwestern

Continued

modeling an established pathogenic mechanism for psoriasis vulgaris. However, imiquimod also likely activates additional pathways, reportedly producing molecular and histopathologic changes suggestive of systemic lupus erythematosus (Liu et al., 2018) and contact dermatitis (Garzorz-Stark et al., 2018).

We sought to understand how single-cell analysis could enhance our understanding of the molecular effects of topical provocations such as oxazolone and imiquimod on the cutaneous immune system. To what extent are inflammatory transcriptional programs shared across related CD45$^+$ subpopulations, rather than being compartmentalized by cell identity? We were especially interested in exploring whether this patterned distribution of such transcriptional responses could be quantitatively described. An in-depth understanding of these molecular signatures might be used to help dissect the causes of pathogenic inflammation in which classical immunopathology or conventional flow cytometry may be limiting, ultimately allowing us to better classify complex skin pathologies in clinical settings such as immunological senescence (Dulken et al., 2019).

RESULTS

Unbiased Classification of Single-Cell Transcriptomes Readily Recapitulates Known, Cutaneous Immune Cell Populations

To explore and compare inflammatory responses, we applied two distinct topical inflammatory agents, oxazolone and imiquimod, in parallel with their vehicle controls, to the ear skin of C57BL/6J mice. Each of the four treatments was applied over the course of a week, and each treatment condition was performed on three different mice (biological replicates, see Transparent Methods for details). We refer to these triplicate samples hereafter as OXA-C (oxazolone control), OXA (oxazolone), IMQ-C (imiquimod control), and IMQ (imiquimod). For each replicate, two ~0.5 × 1.0-cm samples of treated ear skin were harvested 24 h after the last challenge. Histological analysis revealed an acanthotic epidermis with parakeratosis and spongiosis and a dermal inflammatory infiltrate with oxazolone treatment, whereas imiquimod-treated skin displayed an acanthotic epidermis with mounds of parakeratosis, underlying attenuation of the granular layer, and a dermal inflammatory infiltrate (Figure S1A). We enzymatically digested these skin samples, flow sorted for individual CD45$^+$ cells, and then performed scRNA-seq using droplet-based microfluidics (10X Genomics). The number of total single cells initially isolated from each treatment condition was OXA-C: 20,120; OXA: 21,316; IMQ-C: 10,247; and IMQ: 7,632 (Table S1).

Using Seurat (Stuart et al., 2019), data were log-normalized and canonical correlation analysis was performed using 3,000 input variable genes to identify integration anchors among the four different treatment datasets (see Transparent Methods for details). Following integration, dimensional reduction and unsupervised Louvain modularity-based clustering was performed on 59,315 total cells to yield 21 initial cell clusters (see Methods). Visualizing these subpopulations using t-distributed stochastic nearest neighbor embedding (t-SNE, Figure S1B) confirmed their distinct identities. To define these populations, we utilized the Seurat FindAllMarkers and FindConservedMarkers functions (Stuart et al., 2019), which combine p values using meta-analysis methods to identify differentially expressed genes between clusters (conserved across treatment conditions for the latter function; Table S2). After thus identifying transcripts enriched in and typifying each of our 21 initial cell classes (p.adj <0.05), we manually assigned class identity based on comparison to well-established marker genes (Table S3). We excluded small numbers of apparent contaminant keratinocytes expressing high levels of *Krt15*, *Col17a1*, *Krt2*, *Krt5*, and *Krt17*; fibroblasts expressing *Col1a2*, *Col1a1*, *Col3a1*, *Col6a1*, *Col6a2*, and *Col6a3*; and endothelial cells expressing *Selp*, *Sele*, *Cdh5*, *Cd34*, and *Cd93* (Hughes et al., 2019) (Figure S1B and Table S2). We also observed, as have others, that actively dividing cells cluster independently, regardless of cell identity, because of the large number of shared mitotic transcripts (Hsiao et al., 2019). Dividing cells were represented in our data by three groupings with elevated expression of *Pclaf*, *Top2a*, *Mrc1*, *Mki67*, *Birc5*, and numerous histone genes. Finally, we also excluded two other small CD45+ groupings. The first was enriched in the lncRNAs *Gm42418* and *Gm26917* associated with ribosomal RNA contamination. The second was characterized by only a few transcripts (*Neb, Ppp1r16b, Rora, Odc1, Uhrf2, Fnbp1*), for which a clear immune cell class could not be defined (Figure S1B and Table S2).

These exclusions produced 13 distinct immune cell subpopulations, each showing robust representation across both our oxazolone and imiquimod induction and control treatments (Figures 1A and 1B Tables S3 and S5). Six cell classes harbored markers, such as MHC II transcripts, suggestive of antigen-presenting cells (APCs). One subpopulation appeared consistent with macrophages ("Mac"), based on its expression

School of Medicine, Chicago, IL, USA

[12]Veterans Affairs Medical Center, San Diego, CA, USA

[13]These authors contributed equally

[14]These authors contributed equally to this work and share senior authorship

[15]Lead Contact

*Correspondence: raymond.cho@ucsf.edu (R.J.C.), jeffrey.cheng@ucsf.edu (J.B.C.)

https://doi.org/10.1016/j.isci.2020.101582

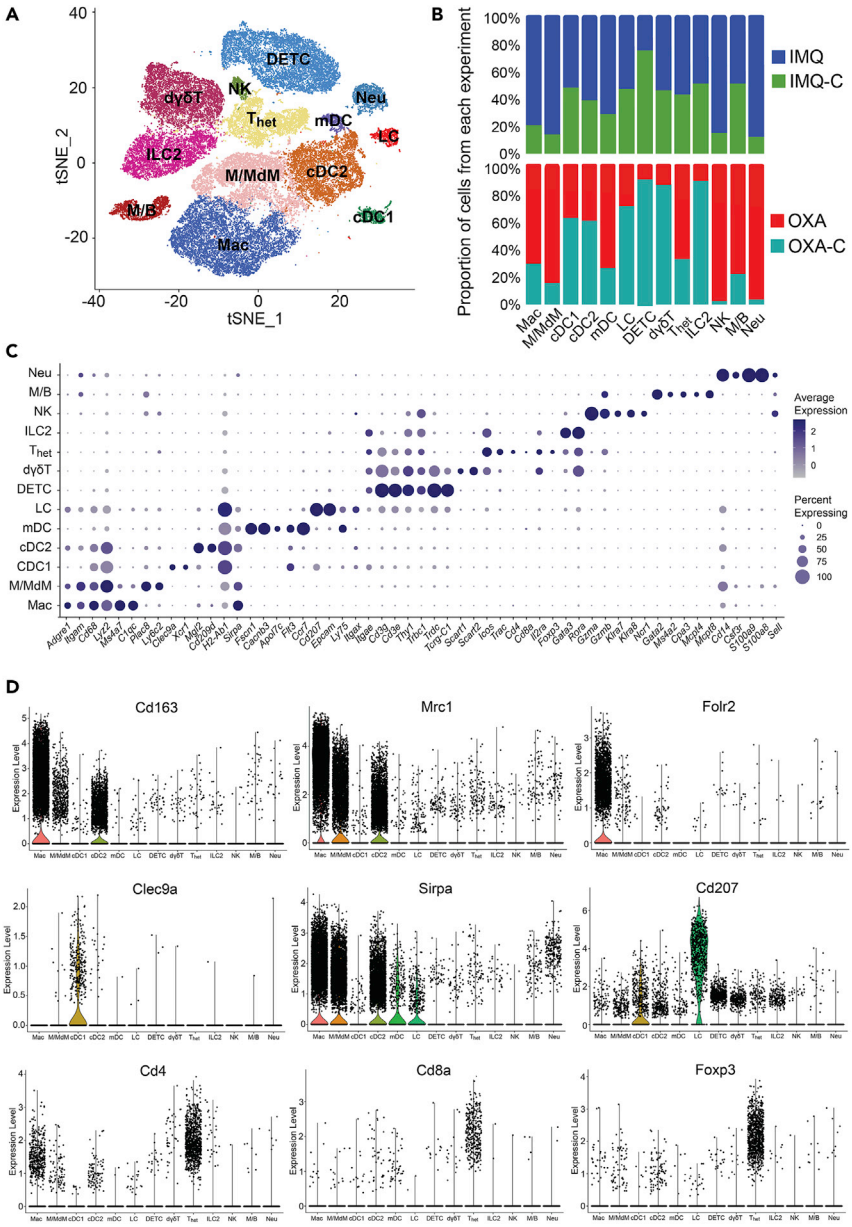

Figure 1. Single-Cell Profiling Demarcates Key Immune Cell Populations in Murine Skin

(A) t-SNE map shows 13 immune cell classes conserved across treatment conditions, delineated by Louvain clustering. Each dot represents one of 44,130 profiled cells.

(B) Relative proportions for each immune cell population for each paired treatment condition and its control. Top panel shows imiquimod (IMQ, blue), and imiquimod control (IMQ-C, green). Bottom panel shows oxazolone (OXA, red) and oxazolone control (OXA-C, turquoise).

(C) Immune cell population marker transcript expression levels (x axis) for the 13 immune cell populations (y axis). Size of dots represents the fraction of cells expressing a particular marker, and color intensity indicates mean normalized scaled expression levels.

(D) Violin plots show normalized transcript expression distribution on a per cluster basis for selected immune cell population marker genes that distinguish major populations. *Cd163*, *Mrc1*, and *Folr2* for macrophages; *Clec9a* for cDC1; *Sirpa* in macrophages, monocytes, and cDC2; *Cd207* for LC; and *Cd4*, *Cd8a*, and *Foxp3* for T_{het}. Each dot represents gene expression of a single cell, and the kernel density plot shape represents the overall distribution.

See also Figure S1 and Tables S1, S2 and S3.

of *Adgre1*, *Itgam*, *Fcgr1*, and *Cd68* (Yu et al., 2016). This population also expresses the so-called tissue-remodeling macrophage markers (similar to a class also referred to as M2 macrophages or alternatively activated macrophages) such as *Cd163*, *Mrc1*, *Folr2,* and intermediate levels of *Arg1* and *Chil3* (Rőszer, 2015) (Figures 1C, 1D, and S2 and Tables S2 and S3). The second cluster appears to represent a combination of monocytes and monocyte-derived macrophages (designated as "M/MdM" in this report). This population expresses not only macrophage markers (*Adgre1*, *Fcgr1*, *Itgam*) but also monocyte markers (e.g., *Lyz2, Ly6c2, Plac8,* and *Cd14*) (Figures 1C and S2 and Tables S2 and S3). A smaller population of cells with elevated *Cd207, Cd24a,* and *Epcam* expression defines Langerhans cells (referred to hereafter as "LC"; Figures 1C, 1D, and 2A and Tables S2 and S3).

The three remaining APC populations display increased expression of *H2-Ab1*, *H2-Eb1*, and *Flt3* and lack the monocyte/macrophage marker *Fcgr1* and are consistent with dendritic cells. To better understand these three populations, we identified differentially expressed genes for each, in comparison with the aforementioned macrophage and Langerhans cell classes. One subpopulation shows elevated *Xcr1, Irf8,* and *Clec9a* and absence of *Irf4, Itgam*, and *Sirpa,* identifying them as likely conventional type 1 dendritic cells (referred to hereafter as "cDC1") (Kashem et al., 2017) (Figures 1C, 1D, and S2 and Tables S2 and S3). A second population showed upregulated transcripts consistent with conventional type 2 dendritic cells (cDC2s), including *Mgl2, Sirpa*, *Itgam*, and *Irf4,* and absence of cDC1 markers (*Irf8, Batf3,* and *Cd207*) (Figures 1C, 1D, and S2 and Tables S2 and S3). The third population is characterized by elevated migration and activation markers *Fscn1*, *Cacnb3, Ccr7, Cd40, Tmem123,* and *Cd274,* demarcating a group of migratory/mature dendritic cells (referred to hereafter as "mDC") (Bros et al., 2011; Ma and Clark, 2009; Riol-Blanco et al., 2005; Takekoshi et al., 2010; Versteven et al., 2018; Yamakita et al., 2011; Figures 1C and S2 and Tables S2 and S3).

Of the remaining seven non-APC CD45$^+$ cell classes, three harbored elevated *Cd3e/g* expression suggestive of T cells. The first of these classes was characterized by high relative expression of *Cd3e/g*, *Trdc*, *Tcrg-C1*, *Thy1*, *Nkg7*, *Fcer1g*, and *Il2rb*, and lack of *Cd4*/*Cd8a* expression, consistent with dendritic epidermal T cells (DETCs), a population of embryonically derived, tissue-resident γδ T cell receptor-expressing cells that function in cutaneous immune surveillance (O'Brien and Born, 2015; Turchinovich and Pennington, 2011) (Figures 1C, 1D, and 2A and Tables S2 and S3). We identified a second cluster as dermal γδ T cells (dγδT) based on strong *Rora* expression and intermediate expression of *Cd3e/g*, *Trdc*, and *Tcrg-C1/2/4*, as well as expression of either *Scart1* (*Cd163l1;* indicative of Vγ6 cells) or *Scart2* (*5830411N06Ri;* indicative of Vγ4 cells) and lack of *Cd4* and *Cd8a* expression (Tan et al., 2019) (Figures 1C, 1D, and 2A and Tables S2 and S3).

The remaining T cell cluster was consistent with αβ T cells displaying broad expression of *Cd3d, Trac, Trbc1, Cd4*, and *Foxp3*, suggesting a heterogeneous mix of T regulatory and conventional *Cd4*$^+$ cells. We thus denoted this category as "heterogeneous T cells," or T_{het} (Figures 1C and 1D, and S2 and Tables S2 and S3). To better define this mixed T_{het} population, we executed a transcriptional gating strategy based on classic T cell markers (see Methods) and were able to identify *Foxp3*$^+$ Tregs, conventional *Cd4*$^+$ *Foxp3*$^-$ T cells (Tconv), *Cd8*$^+$ T cells, and double-negative T cells (Figure S4; Table S5).

We identified another cluster as type 2 innate lymphoid cells (ILC2) based on high expression of the transcription factors *Gata3, Rora, Thy1*, as well as *Il7r, Il5,* and *Il13* coupled with very low levels of *Cd3d/e/g, Eomes, Rorc, Tbx21, and Cd4* (Figures 1C, 1D, and S2 and Tables S2 and S3). This group was also negative for natural killer (NK) and NK T cell markers, e.g., *Klra7, Klra8,* and *Klrb1* (Haug et al., 2019; Juvet and Zhang, 2012; Dutton et al., 2018; Vivier et al., 2018) (Figure S2). An NK cluster with increased relative expression of NK markers, e.g., *Gzma, Klra8, Klra7, Klrb1c (NK1.1), Eomes, Ncr1* was identified (Figures 1C, 1D, and S2 and Tables S2 and S3). Finally, a population of granulocytes likely composed of both mast cells and basophils (hereafter referred to as "M/B") was defined by *Gata2, Ms4a2, Kit, Mcpt4, Itgam,* and *Mcpt8* expression (Figures 1C and S2 and Tables S2 and S3; Li et al., 2015), whereas neutrophils, termed "Neu", were typified by *Cd14*, *S100a8*, *S100a9, Csf3r, Cebpd, Slc11a,* and *Spi1* (Park et al., 2018).

Epitope and Biaxial Transcript Analysis Validate and Refine Transcriptional Classification

To compare transcript-based immune cell classifications with more traditional surface epitope-based approaches (e.g., flow cytometry or CyTOF), we utilized Cellular Indexing of Transcriptomes and Epitopes by Sequencing (CITE-seq) on the OXA-C and OXA samples to quantitate single cell-level protein expression utilizing a sequencing-based output (Stoeckius et al., 2017). We bioinformatically "gated" populations

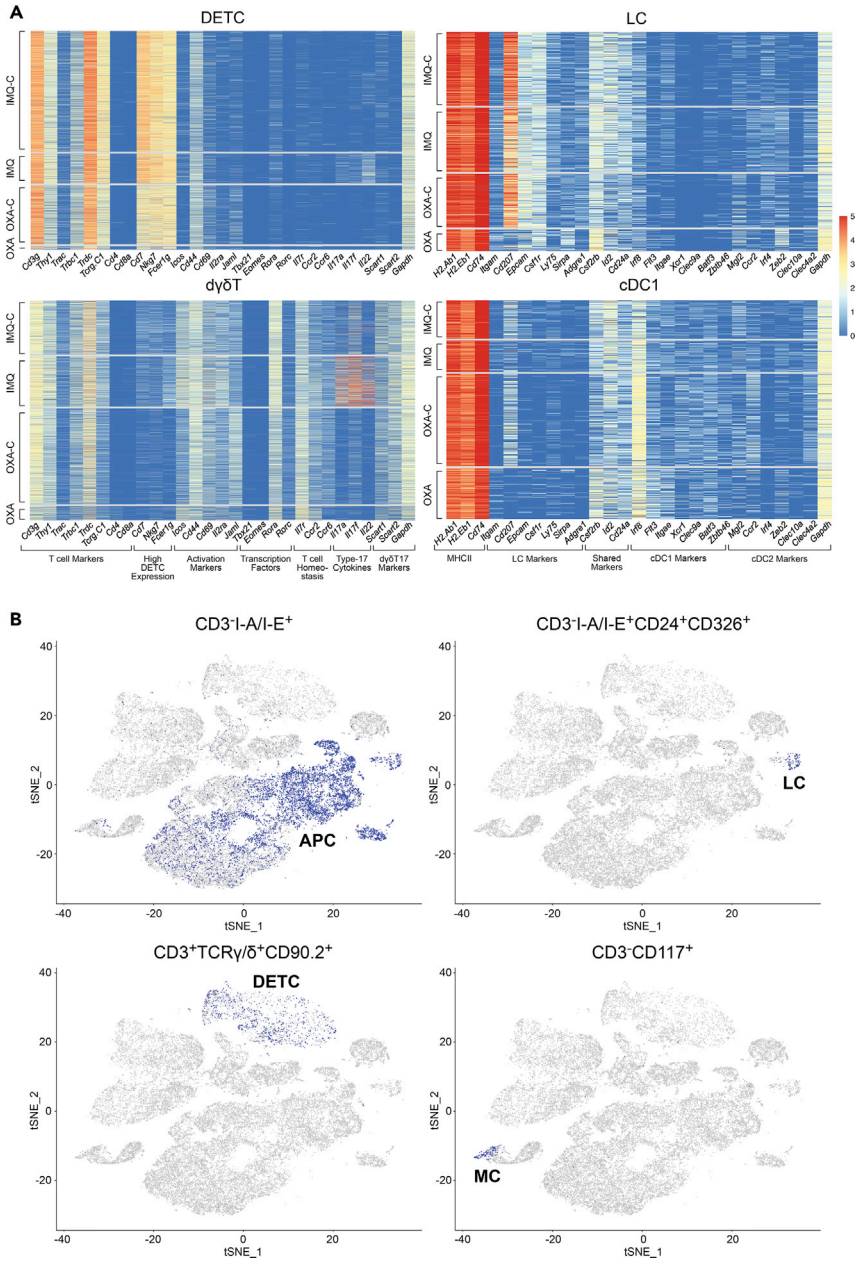

Figure 2. Cluster-Specific Single-Cell Transcript and Protein Expression Validates Immune Cell Population Assignments

(A) Cluster-specific heatmaps show normalized RNA expression count values of selected marker genes on the x axis and single cells on the y axis. Cells are ordered on y axis by treatment condition (IMQ-C, IMQ, OXA-C, OXA).

(B) Projection of protein epitope (CITE-seq) expression "gated" immune cell populations from OXA-C/OXA datasets onto transcript-based t-SNE plot from Figure 1A. Depicted are $CD3^{-}$I-A/I-E^{+} APC cells, $CD3^{-}$I-A/I-$E^{+}CD24^{+}CD326^{+}$ Langerhans cells, $CD3^{+}TCR\gamma/\delta^{+}CD90.2^{+}$ DETCs, and $CD3^{-}CD117^{+}$ mast cells.

See also Figure S2 and Tables S2 and S3.

based on CITE-seq expression to define protein epitope-based cell populations (Zhang et al., 2020), as would be done with flow cytometry, and overlaid these on our transcript-based clusters. Consistent with our APC transcript based-assignments (Mac, M/MdM, cDC1, cDC2, mDC, and LC), we find strong overlap with $CD3^{-}$I-A/I-E^{+} CITE-seq gated cells (Figure 2B). $CD3^{-}$I-A/I-$E^{+}CD24^{+}CD326^{+}$ cells localize to the transcript-defined LC population. $CD3^{+}TCR\gamma/\delta^{+}CD90.2^{+}$ cells show ample representation within the

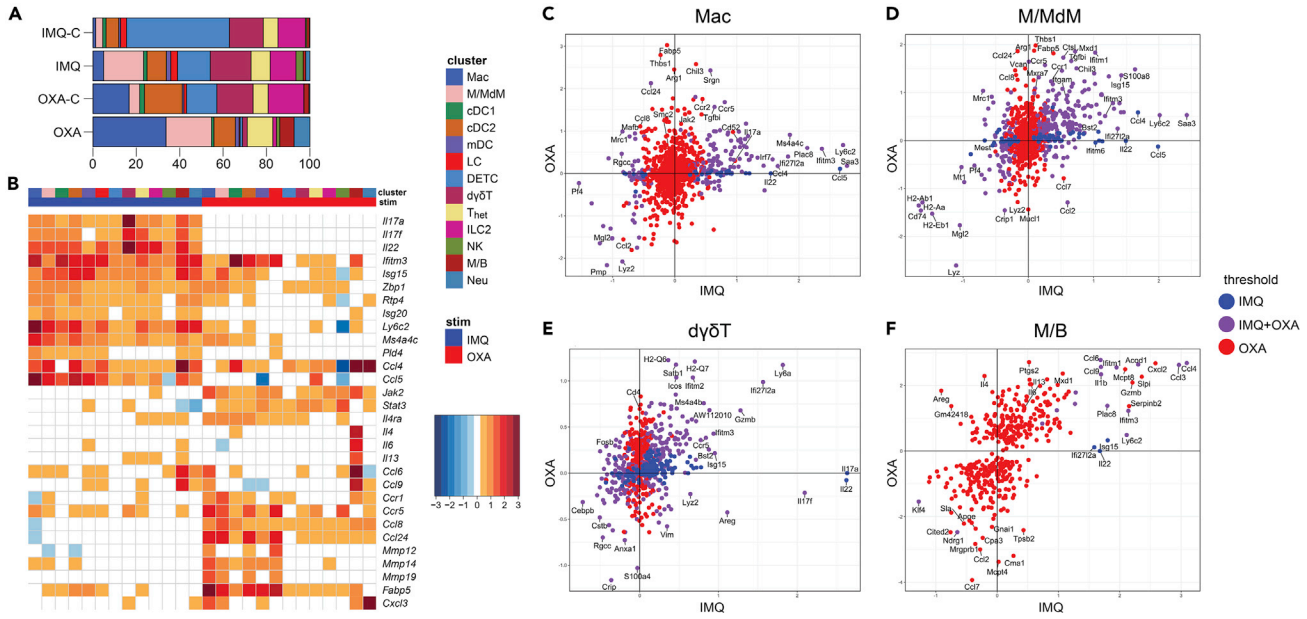

Figure 3. Oxazolone and Imiquimod Divergently Reprogram Immune Cells

(A) Stacked bar plots showing relative percentages of each immune cell population for each of the treatment conditions (IMQ-C, IMQ, OXA-C, and OXA).

(B) Unsupervised hierarchical clustering heatmap for treatment-induced differentially expressed genes on a per cluster basis. Columns depict average logFC of oxazolone- or imiquimod-treated cells (versus control) for each cluster. Rows depict selected treatment-specific DEGs for OXA versus OXA-C and IMQ versus IMQ-C.

(C–F) (C) Cluster-specific scatterplots showing OXA or IMQ treatment-induced differentially expressed genes for macrophages, (D) M/MdM cells, (E) dγδT cells, and (F) M/B populations (avg_logFC for OXA DEGs relative to OXA-C on y axis and IMQ DEGs relative to IMQ-C on x axis). Pseudocolored dots represent significant DEGs (p.adj <0.05) for OXA (red), IMQ (blue), or both treatments (purple).

See also Figures S3 and S4 and Tables S4 and S5.

RNA-based DETC cluster but not dγδT cells (which show lower γ/δ expression than DETCs). The transcript-based mast cell population harbors $CD3^{-}CD117^{+}$-expressing cells (Figure 2B).

Oxazolone or Imiquimod Treatment Induce APC-Dominant Shifts into Mouse Skin

Although the OXA and IMQ datasets contained the same basic cell types, their composition by type showed substantial differences. To evaluate the relative abundance of 13 immune cell types in two conditions, we examined the percentage of each subpopulation in each of the OXA-C, OXA, IMQ-C, and IMQ datasets (Figure 3A and Table S5). However, because a subpopulation can only be assessed as a proportion of total cells in a given profile, it is not possible to formally ascertain if changes in population abundance represent absolute increased numbers of a cell type or relative decreases in other major cell types. Therefore, the largest shifts are more likely to represent new, infiltrating cells during treatment. Imiquimod and oxazolone both lead to marked increase in relative percentages of macrophage (102% and 273% for OXA and IMQ, respectively), M/MdM (340% and 476%), mDC (133% and 147%), NK (2,087% and 44%), and neutrophil (1,643% and 555%) cells. Population shift decreases after oxazolone treatment include dermal γδ T cells (−87%), ILC2 (−90%), and LC (−65%), as well as decreases for DETC for both oxazolone (−92%) and imiquimod (−68%) (Figure 3A and Table S5).

Oxazolone and Imiquimod Divergently Reprogram $CD45^{+}$ Cell Transcriptomes toward JAK2 or Interferon Responses

Our initial classification of $CD45^{+}$ single-cell transcriptomes into 13 subpopulations conflates some immune cell populations that are differentiated through classical serial gating strategies, particularly for T cell classes. However, we hypothesized that transcriptional commonalities and differences in these initial classes would enable an informative, high-level survey of gene expression differences caused by oxazolone and imiquimod. We compared transcripts differentially expressed (avg_logFC >0.5, p.adj <0.05) in either treatment condition in at least one cluster (1,088 transcripts in total, Figures 3B and S3A). This approach

immediately accentuated striking treatment- and cluster-specific transcriptional shifts. Globally, IL17/22 and IFN-γ signatures emerge in multiple subpopulations after imiquimod treatment. In contrast, oxazolone generates a more complex picture, with upregulation of type 1 and type 2 cytokines, and IFN-responsive genes in selected cell classes, consistent with previous reports (Liu et al., 2019; Pantelyushin et al., 2012; Thomson et al., 1993; Wenzel et al., 2005) (Figures 3B, S3A, and S3B and Table S4).

The widespread IMQ-specific induction of *IL17a, Il17f,* and *Il22* transcripts is most robust in dγδT cells (Figures 3B, 3E, and S3A and Table S4). We also observe pervasive upregulation of interferon-responsive genes, including a gene cluster composed of *Ifitm3, Isg15, Zbp1, Rtp4, and Isg20* as well as transcripts not classically known to be interferon responsive (*e.g., Ly6c2, Ms4a4c, and Pld4*). This interferon signature is most prominent in imiquimod-treated APC populations (such as Mac, M/MdM, and cDC2) and seen only faintly in the corresponding oxazolone-treated APC populations (Figures 3B, S3A, and S3B and Table S4). Imiquimod also upregulates chemokines associated with type 1 inflammatory responses (*Ccl4* and *Ccl5*) most prominently in M/B cells and APC populations (Figures 3B, 3D, 3F, S3A, and S3B). Oxazolone, in contrast, primarily elevates only *Ccl4*, in M/B cells and neutrophils.

Oxazolone widely elevates *Jak2* and *Stat3* expression, as well as *Il4ra*, effects absent after imiquimod treatment (Figures 3B and S3A and Table S4). Oxazolone-treated cells also show marked upregulation of type 2 cytokine transcripts (*Il4*, *Il6*, *Il13*) and CCR1 chemokine ligands (*Ccl6* and *Ccl9*), most prominently in M/B cells (Figures 3B and 3F and Table S4). We also observe robust upregulation in OXA-treated APC populations of genes such as the *Ccr1* and *Ccr5* chemokine receptors, the *Ccl8* and *Ccl24* beta-chemokines, as well as matrix metalloproteinases (*Mmp12/14/19*) and *Fabp5* (Figures 3B–3D and S3 and Table S4). Except for *Ccr5*, these shifts are nearly absent from the IMQ dataset. The neutrophil chemoattractant *Cxcl3* is also elevated in oxazolone-treated neutrophils (Figures 3B and S3 and Table S4).

To better characterize the effects of imiquimod and oxazolone on the T_{het} cell population, we subsetted these cells based on a transcriptional gating approach into the four T cell types described above: *Foxp3*$^+$ Tregs, conventional *Cd4*$^+$*Foxp3*$^-$ T helper cells (Tconv), *Cd8a/b1*$^+$ T cells, and *Cd4*$^-$*Cd8a/b1*$^-$ double-negative T cells (DNT) (Figure S4 and Tables S4 and S5; Methods) (Gao et al., 2011). We then assessed imiquimod or oxazolone-induced RNA expression changes for the 265 most variable genes, as well as selected type 1, type 2, type 17 cytokine, and interferon response-related genes (Figure S4). We find key treatment-induced differentially expressed genes previously identified in the T_{het} population in all four T_{het} subpopulations, i.e., IMQ-specific upregulation of *Il17a*, *Il17f*, *Il22,* and OXA-specific upregulation of *Jak2* and *Stat3.*

Oxazolone induced a marked increase in the number of Tregs (Table S5), which was accompanied by upregulation of *Ets1* and *Ikzf2,* transcription factors known to both regulate *Foxp3* expression and mediate the suppressive activity of this cell type (Kim et al., 2015; Mouly et al., 2010) (Figure S4, Table S4). In oxazolone-treated cells, there is a trend toward T cell activation gene upregulation in *Cd8*$^+$ cells, e.g., the co-inhibitory receptors *Pdcd1* (*Pd-1*), *Lag3* and *Havcr2* (*Tim-3*), granzyme molecules *Gzma* and *Gzmb,* and *Ccr5* (Okoye et al., 2017; Viola and Luster, 2008) (Figure S4 and Table S4). We also observe OXA-induced upregulation of *Havcr2* in *Cd4*$^+$T cells, comporting with its known expression in CD4$^+$ Th1 cells, where it negatively regulates *IFNG* production (Das et al., 2017; Hastings et al., 2009) (Figure S4 and Table S4).

Imiquimod treatment induced the upregulation of MHC I and interferon response genes across all T cell types, although only *Ifi27l2a* was significant across all T cell subpopulations (Figure S4 and Table S4). Interestingly, the cathepsin *Ctss,* which is known to be expressed in barrier skin cells and is mechanistically implicated in both atopic dermatitis and psoriasis, was strongly upregulated in all imiquimod-treated T cell types (Figure S4 and Table S4; Ainscough et al., 2017; Kim et al., 2012; Schönefuss et al., 2010). Consistent with our transcriptional data, flow cytometry analysis revealed a trend toward increased IL17A and IL22 expression in Tconv, CD8, and dγδT cells, as well as increased CCL5 expression in CD8 and Treg cells with imiquimod treatment (Figure S5).

Basophils Infiltrate Skin as Primary Producers of IL4 and IL13 following Oxazolone but Not Imiquimod Treatment

We observed *Il4* and *Il13* induction mainly restricted to the M/B cluster, which expresses known granulocyte markers (Figure 3 and Table S4). To more deeply understand this phenomenon, we subjected these cells to κ-means clustering, which revealed two distinct classes (Figure 4A). Although M/B granulocyte cells

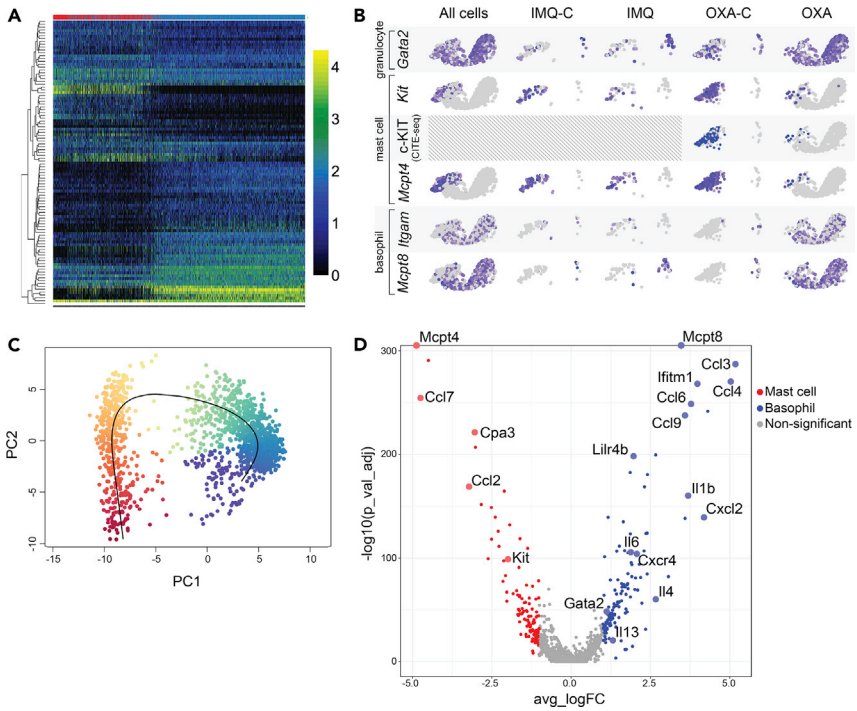

Figure 4. Infiltrating Basophils Produce *Il4* and *Il13* after Oxazolone but Not Imiquimod Treatment of Murine Skin

(A) Heatmap displaying count values for the top 100 most variable genes (y axis) defined by pseudotime (x axis) for M/B population cells. Two nonredundant and non-covariate *k*-means-defined subpopulations are denoted by the color bar at the top of the panel (mast cells, red, left; basophils, blue, right). Rows represent genes and columns represent single cells of the M/B cluster.

(B) Feature plots showing mast and basophil marker expression projected onto the t-SNE M/B cluster from Figure 1A. Each row depicts transcript expression of a different marker gene for mast cells (*c-Kit* RNA and protein [CITE-seq] and *Mcpt4*) and basophils (*Itgam*, *Mcpt8*). Each column shows M/B population t-SNE plots representing only the cells from the treatment condition listed at the top.

(C) Principal-component analysis (PCA) of mast cells (orange/red, left) and basophils (blue/green, right) demonstrating these subpopulations do not share a differentiation trajectory.

(D) Differential gene expression volcano plot between mast cells and basophils. x axis depicts the average logFC for basophils relative to mast cells. y axis depicts –log10(p.adj). Significant genes are defined as $|avg\_logFC| \geq 1$ and p.adj ≤ 0.05 [$-log10(p.adj) \geq 1.3$]. Blue dots represent basophil, and red dots represent mast cell upregulated genes.

See also Table S4.

globally express *Gata2* (Figure 4B), the putative mast cell cluster was clearly demarcated by *Mcpt4* and *Kit* (the latter on both the transcript and epitope levels), whereas the presumptive basophils uniquely expressed *Mcpt8* and *Itgam* (Akahoshi et al., 2011; Siracusa et al., 2013) (Figure 4B). Surprisingly, basophils were found almost exclusively in the OXA dataset, and not in OXA-C, IMQ-C, or IMQ (Figure 4B).

The restriction of basophils to this dataset suggests that they were uniquely induced to infiltrate skin by oxazolone (Figure 4B). Given the transcriptional relatedness of granulocytes, we first evaluated the alternative hypothesis that our putative basophils might instead represent reactive mast cells. Utilizing global lineage structure and inference of pseudotime variables (Street et al., 2018) (Slingshot), we were unable to discern an evolutionary trajectory connecting these subpopulations (Figure 4C). We next analyzed gene expression differences between mast cells (found in both OXA and IMQ) and basophils (found only in OXA). Basophils infiltrating after oxazolone treatment appear not only specifically enriched in key marker transcripts such as *Mcpt8* but also appear to serve as the exclusive source of new *Il4*, *Il6*, and *Il13* (Figure 4D).

Oxazolone Provokes a More Compartmentalized Pattern of Global Transcriptional Response, Relative to CD45$^+$ Cell Identity, Than Imiquimod Stimulation

As noted above, oxazolone activates sharply distinct transcriptional programs in different immune cell types. Imiquimod, in contrast, appears to activate related patterns across multiple populations. One of

the opportunities conferred by single-cell data is the ability to quantitate such differing global molecular responses, allowing their comparison and classification by algorithms. Such approaches could eventually enable us to deduce the mechanism of new sources of inflammation, based solely on analyzing single-cell patterns of immune response and placing them in context of known agents.

As an initial test of this hypothesis, we first systematically identified global, single-cell, transcriptional response patterns produced by oxazolone and imiquimod. We next examined whether these patterns showed simple compartmentalization between our identified immune cell types, or whether they showed more complex distribution throughout our $CD45^+$ subpopulations. In other words, we sought to ask whether the molecular responses to a given agent are wholly defined by immune cell type, or are they more heterogeneously distributed across cell types? We aimed to develop unbiased, quantitative means to make such an assessment.

To technically execute this approach, for each cell in the oxazolone and imiquimod-treated samples, we initially identified one cell in its respective control group with the most similar, harmonized transcriptomic pattern, hypothesizing that this control cell could be used as a proxy for a pre-treatment version of the same cell type (Figure 5A). We only considered control cells that were in the top 50 nearest neighbors. We then calculated gene expression differences over the 1,000 most variable genes between thousands of such pairs of cells, generating a vector of pairwise single-cell gene expression comparisons between a treatment and its control:

$$\mathrm{DiVNCE(Tx)} = \mathit{sctx}\mathrm{(Tx)} - \mathit{sctx}\mathrm{(C(Tx))}$$

where Tx represents a treated cell, C(Tx) represents the nearest control cell, and sctx() is a vector of scaled expression values for 1,000 genes in a given cell. We refer to this library of pairwise comparisons as "Difference Vs. Nearest Control cEll," or "DiVNCE" profiles. The DiVNCE profiles were clustered, producing 11 discrete response signatures for the OXA dataset and 13 for IMQ (Table S6). We next compared DiVNCE patterns for OXA and IMQ against our initial 13 $CD45^+$ cell classifications. This unsupervised approach re-identifies a basophil *Mcpt8*/*Il13* DiVNCE signature in the OXA M/B granulocyte cluster and an *Il17* signature in a subset of IMQ dermal γδ T cells, validating our approach (Figures 5B and S6 and Table S6).

In Figure 5B, the upper left UMAP shows OXA $CD45^+$ cells clustered based on 12 DiVNCE signatures; the upper right panel shows the same cell organization colored by our original 13 $CD45^+$ cell identities. Similarly, the lower left shows the IMQ dataset clustered based on 13 DiVNCE patterns, then colored on the lower right panel by cell identity. It is readily apparent from this representation that DiVNCE signatures more precisely delineate cell identities for OXA than for IMQ. For example, the OXA Mac subpopulation is subdivided into five single-cell DiVNCE subpopulations (MacS1–5), each with distinct inflammatory patterns (Figure 5C). Even in the Mac DiVNCE cluster that includes other APCs groups such as mDC and M/MdM (MacS 5), these other APCs are spatially distinct (Figure 5B), suggesting that they express the MacS 5 pattern differently. Overall, the DiVNCE clusters recapitulate cell identities in the OXA data, in cases at higher resolution. In contrast, APCs in the IMQ data are mixed in five DiVNCE clusters based on interferon response signatures (IRS 1–5) (Figures 5B and 5C). We generated a quantitative measure for positive compartmentalization by calculating the adjusted rand index (ARI) between the DiVNCE cluster assignment and the $CD45^+$ cell type assignments. The ARI for OXA is 0.272, 95% confidence interval (CI) = (0.268–0.275), compared with 0.128, 95% CI = (0.124–0.131) for IMQ, reflecting significantly enhanced compartmentalization of global expression changes in the oxazolone response.

DISCUSSION

We present here one of the first single-cell comparisons of inflammatory responses to distinct provocations in mouse skin. While confirming well-established molecular features of the response to oxazolone and imiquimod, our global $CD45^+$ cell capture also allows us to directly examine the molecular behavior of multiple cell populations, some of which have not been interrogated directly in standard reports. In each of our datasets, we readily identify major APC and T cell classes, many of which we further refine with successive rounds of multiparametric segregation. To validate our transcript-based classifications, we also utilized sequencing-based protein epitope analysis (CITE-seq), which showed strong correlation for transcript- and protein epitope-defined APC, Langerhans cell, DETC, and mast cell populations. This approach validates most functionally important immune cell subpopulations, including DETC and cDC2, as well as Langerhans and mast cells.

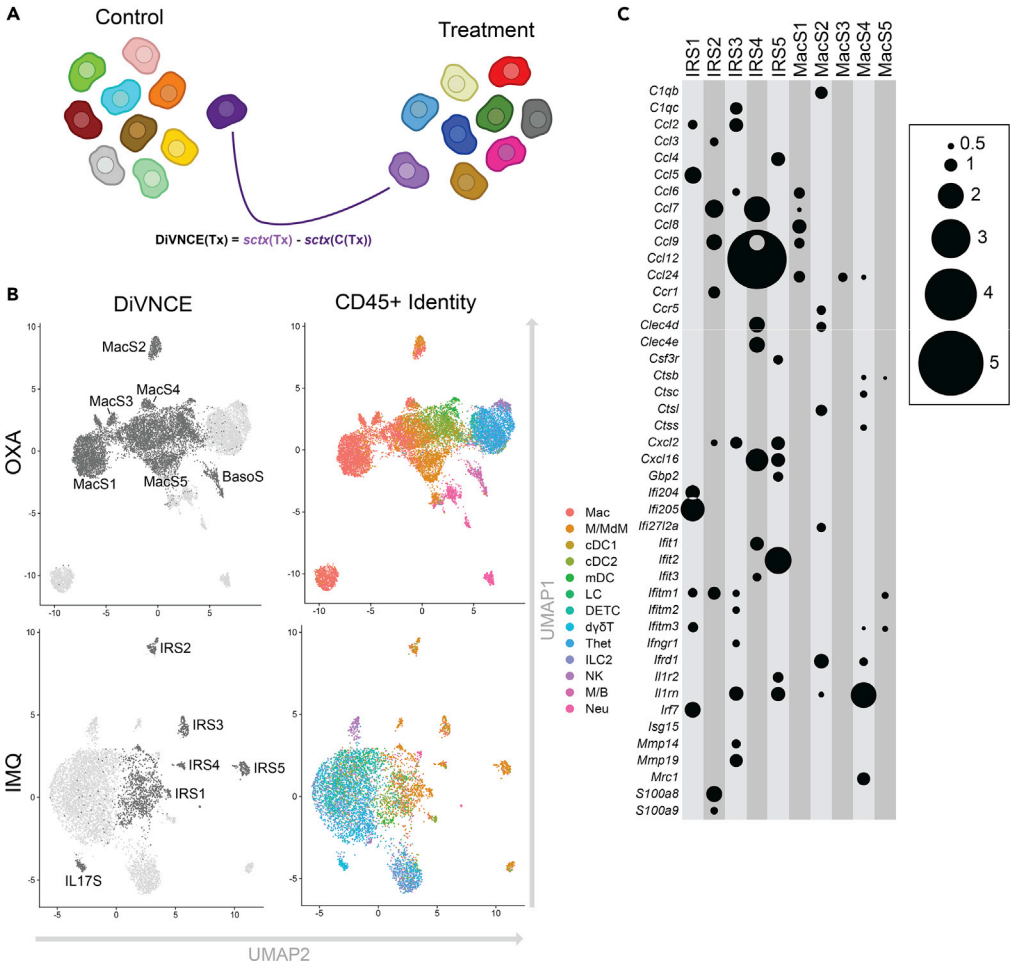

Figure 5. DiVNCE Analysis Yields High Degree of Compartmentalization by Cell Identity for Oxazolone but not Imiquimod Transcriptional Response in CD45$^+$ Cells

(A) Schematic representation by which DiVNCE identifies the most similar, "neighboring" control cell for each treatment cell and then catalogs their transcriptional differences.

(B) UMAP representation showing partitioning of oxazolone-treated cells based on 12 DiVNCE profiles (six highlighted for comparison, upper left panel), with same clusters colored by cell identities as depicted in Figure 1A (upper right). Lower left panel shows imiquimod-treated cells partitioned on 11 DiVNCE profiles (six highlighted for comparison) and same clusters colored by cell identity (lower right). Mac clusters 1–5 represent five DiVNCE patterns finely subdividing macrophages in the Mac classification, highlighting greater compartmentalization. In contrast, in the IMQ dataset, interferon-responsive DiVNCE signatures (IRS 1–5) are each shown by multiple APC types, showing mixing and lower relative compartmentalization. Also displayed for validation are unbiased detection of a basophil *Mcpt8*/*Il13* DiVINCE signature in the OXA M/B granulocyte cell identity cluster and an *IL17* signature in a subset of IMQ dermal γδ T cells (Figure S6 and Table S6).

(C) Log2-fold elevations from DiVNCE comparisons (represented by circle size) for inflammatory transcripts (*y* axis) for MacS S and IRS signatures (x axis), all p.adj <1 × 10^{-3}.

See also Figure S5 and Table S6.

These single cell profiles offer unprecedented resolution in dissecting divergent cutaneous inflammatory immune response. Continuous oxazolone application is classically associated with immediate type hypersensitivity followed by a shift toward production of Th-2-associated cytokines (Man et al., 2008; Wang et al., 2000). Oxazolone has been used to model both allergic contact dermatitis and atopic dermatitis, although transcriptomic studies suggest that IL23 injection more closely resembles the latter (Ewald et al., 2017). Our data was striking for elevation of *Jak2* and *Stat3* expression in most CD45$^+$ cell populations, suggesting that a global activation of this pathway is central to some instances of allergic contact dermatitis. Successful JAK inhibition of the oxazolone response has been observed previously, primarily using JAK3-selective agents

(Fujii and Sengoku, 2013; Mahajan et al., 2015), leaving open the possibility that JAK2-selective agents may be even more effective in counteracting a subset of delayed-type hypersensitivity.

While granulocytes have long been known to be generally capable of *Il4* and *Il13* production (Gessner et al., 2005), our analyses demonstrate the power of scRNA-seq to precisely differentiate cell identity and demarcate transcript expression as a function of that cell identity. Our single-cell analyses detect newly arriving basophils after oxazolone treatment, which then appear to serve as the sole detectable source of elevated *Il4* and *Il13* production. The restriction of this induction to infiltrating basophils is nearly complete, echoing type 2 results in human patients with atopic dermatitis (Mashiko et al., 2017). Thus, agents inhibiting basophil migration or activity may be especially useful in ameliorating some type 2 responses. Although mast cells are known to produce these type 2 cytokines under some conditions, they do not demonstrate this role in our study. Imiquimod provokes no comparable *Il4* or *Il13* production. Future investigation will determine whether other inducers of delayed-type hypersensitivity produce a similar profile, or whether the landscape of type 2 cytokines production is instead antigen-specific.

Topical provocation with imiquimod is known to produce *Il17*, mainly from *IL23*-induced Th17 cells (Zheng et al., 2007). More recently, skin γδT cells, mainly Vγ4$^+$ γδT cells, as well as Rorγt$^+$ ILCs cells, have been established to produce *Il17a, Il17f, and Il22* (Pantelyushin et al., 2012). Consistent with these reports, we detect dγδT cells as the main producer of these cytokines (Figure 3A), but there is also significant *Il17/Il22* production by Vγ6$^+$ γδT cells (Figure 2A). Along with type 17 cytokine upregulation in macrophage, M/MdM, and T_{het} cell subpopulations, our data suggest that imiquimod impacts target tissue through a broader set of immune cells than previously appreciated.

We also observed the pan-upregulation of *Ccl4* and *Ccl5* in most imiquimod-treated CD45$^+$ subpopulations, a less-described phenomenon. A recent study indicates that these cytokines may also be involved intimately in the imiquimod response, quenching inflammation through Treg recruitment (Oka et al., 2017). However, *Ccl5* and *Ccr5* (encoding the receptor for both CCL4 and CCL5 ligands) are upregulated in human psoriasis and downregulated after treatment, supporting a role in pathogenicity. The discrepancy may derive from the differences between humans and mice (Mack et al., 2001), as well as complex ligand-receptor interactions between CCL4/CCL5 and CCR1/CCR3. Further work will be required to deconvolute these roles.

We describe and demonstrate a novel method, DiVNCE, that quantitatively describes discrete expression programs generated by stimuli and allows us to assess their distribution among immune cell populations. We show that whereas oxazolone produces a highly cell type-specific pattern, imiquimod enforces a more heterogeneous response in T cells, consisting of multiple, distinct, interferon-related programs (Figure 5B). Interestingly, APCs show greater plasticity in response to the agents in this study than T cell subpopulations. We describe and apply the ARI metric, which quantitates this greater degree of molecular response compartmentalization for oxazolone at statistical significance. Even more nuanced pattern-based matching approaches may allow the immunological consequences of new chemical agents to be rapidly assessed by comparison against a library of existing compounds. Further investigation, based on profiling additional types of immune stimulation, will be required to validate and extend our findings.

Limitations of the Study

Transcriptional similarity-based single-cell computational classification may lead to conflation of similar immune cell types. In particular, this was noted in the heterozygous T cell and mast/basophil populations, which required further computational subdivision to identify cell populations that better correlate with classic flow cytometry-defined populations. Furthermore, the inherent biases of droplet-based scRNA-seq and utilization of RNA expression for immune cell type classification will lead to variation from protein epitope-based flow cytometry-defined populations.

Large treatment-induced increases in APC populations and their known anatomic site-specific diminishment in mouse cutaneous ear led to a relative paucity of certain T cell subtypes (e.g., CD4, CD8, Treg). Consequently, statistical power for analyses with these populations was limited.

Resource Availability

Lead Contact

Further information and requests for resources should be directed to and will be fulfilled by the Lead Contact, Jeffrey Cheng (jeffrey.cheng@ucsf.edu).

Materials Availability

This study did not generate new unique reagents.

Data and Code Availability

Single-cell RNA-seq data have been deposited in the NIH Gene Expression Omnibus (GEO) database, under accession number GSE149121. All statistical analysis and plotting of scRNA-seq and cell surface protein data were performed using Rstudio software (Version 1.2.5033). All analysis scripts are available upon request to corresponding authors.

METHODS

All methods can be found in the accompanying Transparent Methods supplemental file.

SUPPLEMENTAL INFORMATION

Supplemental Information can be found online at https://doi.org/10.1016/j.isci.2020.101582.

ACKNOWLEDGMENTS

We acknowledge Rachel M. Sevey for critical assistance in scientific graphic design, Paola DiMeglio for assistance in antibody selection, and support from the San Diego CFAR Genomics and Sequencing core. This project was supported in part by National Institute of Arthritis and Musculoskeletal and Skin Diseases of the National Institutes of Health K08AR067243 to J.B.C., K08AR074556 to M.S.F., R01AR061106 to T.M.M. (administered by the Northern California Institute for Research and Education), NIH R01CA163336 to J.S.S., and VA Career Developmental Award CDA-2 (IK2BX002731) to N.B.B. This content is solely the responsibility of the authors and does not necessarily represent the official views of either the National Institutes of Health or the Department of Veterans Affairs.

AUTHOR CONTRIBUTIONS

R.J.C. and J.B.C. designed the study. Y.L., C.C., P.H., W.Z., M.S.F., and R.R.G. performed sample preparation and analysis. Y.L, C.C., A.J.S., S.Z., M.A.T., J.L., N.B.-B., S.C.B., and J.S.S. performed computational analyses. J.P.N. performed microscopy analyses. Y.L, C.C., R.J.C., and J.B.C. wrote the manuscript with contributions from A.J.S., S.Z., M.S.F, R.R.R.-G., P.H., S.W.K., S.H., J.R.L., J.P.N., M.A.M, W.Z., M.-Q.M., T.M.M., A.C., N.B., S.C.B., R.G., D.H.K., K.K., J.C., and J.S.S.

DECLARATION OF INTERESTS

A.J.S. and S.C.B. are employees of ImmunityBio Inc, S.C.B. is an equity holder of ImmunityBio Inc. The remaining authors disclose no conflicts.

Received: August 12, 2020
Revised: September 12, 2020
Accepted: September 16, 2020
Published: October 23, 2020

REFERENCES

Ainscough, J.S., Macleod, T., McGonagle, D., Brakefield, R., Baron, J.M., Alase, A., Wittmann, M., and Stacey, M. (2017). Cathepsin S is the major activator of the psoriasis-associated proinflammatory cytokine IL-36γ. Proc. Natl. Acad. Sci. U S A *114*, E2748–E2757.

Akahoshi, M., Song, C.H., Piliponsky, A.M., Metz, M., Guzzetta, A., Abrink, M., Schlenner, S.M., Feyerabend, T.B., Rodewald, H.-R., Pejler, G., et al. (2011). Mast cell chymase reduces the toxicity of Gila monster venom, scorpion venom, and vasoactive intestinal polypeptide in mice. J. Clin. Invest. *121*, 4180–4191.

Bros, M., Dexheimer, N., Ross, R., Trojandt, S., Höhn, Y., Tampe, J., Sutter, A., Jährling, F., Grabbe, S., and Reske-Kunz, A.B. (2011). Differential gene expression analysis identifies murine Cacnb3 as strongly upregulated in distinct dendritic cell populations upon stimulation. Gene *472*, 18–27.

Cheng, J.B., Sedgewick, A.J., Finnegan, A.I., Harirchian, P., Lee, J., Kwon, S., Fassett, M.S., Golovato, J., Gray, M., Ghadially, R., et al. (2018). Transcriptional programming of normal and inflamed human epidermis at single-cell resolution. Cell Rep. *25*, 871–883.

Croft, A.P., Campos, J., Jansen, K., Turner, J.D., Marshall, J., Attar, M., Savary, L., Wehmeyer, C., Naylor, A.J., Kemble, S., et al. (2019). Distinct fibroblast subsets drive inflammation and damage in arthritis. Nature *570*, 246–251.

Das, M., Zhu, C., and Kuchroo, V.K. (2017). Tim-3 and its role in regulating anti-tumor immunity. Immunol. Rev. *276*, 97–111.

Dudeck, A., Dudeck, J., Scholten, J., Petzold, A., Surianarayanan, S., Köhler, A., Peschke, K., Vöhringer, D., Waskow, C., Krieg, T., et al. (2011). Mast cells are key promoters of contact allergy that mediate the adjuvant effects of haptens. Immunity *34*, 973–984.

Dulken, B.W., Buckley, M.T., Navarro Negredo, P., Saligrama, N., Cayrol, R., Leeman, D.S., George, B.M., Boutet, S.C., Hebestreit, K., Pluvinage, J.V., et al. (2019). Single-cell analysis reveals T cell infiltration in old neurogenic niches. Nature *571*, 205–210.

Dutton, E.E., Camelo, A., Sleeman, M., Herbst, R., Carlesso, G., Belz, G.T., and Withers, D.R. (2018). Characterisation of innate lymphoid cell populations at different sites in mice with defective T cell immunity. Wellcome Open Res. *2*, 117.

Ewald, D.A., Noda, S., Oliva, M., Litman, T., Nakajima, S., Li, X., Xu, H., Workman, C.T., Scheipers, P., Svitacheva, N., et al. (2017). Major differences between human atopic dermatitis and murine models, as determined by using global transcriptomic profiling. J. Allergy Clin. Immunol. *139*, 562–571.

Fujii, Y., and Sengoku, T. (2013). Effects of the Janus kinase inhibitor CP-690550 (tofacitinib) in a rat model of oxazolone-induced chronic dermatitis. Pharmacology *91*, 207–213.

Gao, J.F., McIntyre, M.S.F., Juvet, S.C., Diao, J., Li, X., Vanama, R.B., Mak, T.W., Cattral, M.S., and Zhang, L. (2011). Regulation of antigen-expressing dendritic cells by double negative regulatory T cells. Eur. J. Immunol. *41*, 2699–2708.

Garzorz-Stark, N., Lauffer, F., Krause, L., Thomas, J., Atenhan, A., Franz, R., Roenneberg, S., Boehner, A., Jargosch, M., Batra, R., et al. (2018). Toll-like receptor 7/8 agonists stimulate plasmacytoid dendritic cells to initiate TH17-deviated acute contact dermatitis in human subjects. J. Allergy Clin. Immunol. *141*, 1320–1333.e11.

Gessner, A., Mohrs, K., and Mohrs, M. (2005). Mast cells, basophils, and eosinophils acquire constitutive IL-4 and IL-13 transcripts during lineage differentiation that are sufficient for rapid cytokine production. J. Immunol. *174*, 1063–1072.

Hastings, W.D., Anderson, D.E., Kassam, N., Koguchi, K., Greenfield, E.A., Kent, S.C., Zheng, X.X., Strom, T.B., Hafler, D.A., and Kuchroo, V.K. (2009). TIM-3 is expressed on activated human CD4+ T cells and regulates Th1 and Th17 cytokines. Eur. J. Immunol. *39*, 2492–2501.

Haug, T., Aigner, M., Peuser, M.M., Strobl, C.D., Hildner, K., Mougiakakos, D., Bruns, H., Mackensen, A., and Völkl, S. (2019). Human double-negative regulatory T-cells induce a metabolic and functional switch in effector T-cells by suppressing mTOR activity. Front. Immunol. *10*, 883.

Hsiao, C.J., Tung, P., Blischak, J.D., Burnett, J.E., Barr, K.A., Dey, K.K., Stephens, M., and Gilad, Y. (2019). Characterizing and inferring quantitative cell cycle phase in single-cell RNA-seq data analysis. bioRxiv, 526848.

Hughes, T.K., Wadsworth, M.H., Gierahn, T.M., Do, T., Weiss, D., Andrade, P.R., Ma, F., Silva, B.J.de A., Shao, S., Tsoi, L.C., et al. (2019). Highly efficient, massively-parallel single-cell RNA-seq reveals cellular states and molecular features of human skin pathology. BioRxiv, 689273.

Jordão, M.J.C., Sankowski, R., Brendecke, S.M., Sagar, Locatelli, G., Tai, Y.-H., Tay, T.L., Schramm, E., Armbruster, S., Hagemeyer, N., et al. (2019). Single-cell profiling identifies myeloid cell subsets with distinct fates during neuroinflammation. Science *363*, eaat7554.

Juvet, S.C., and Zhang, L. (2012). Double negative regulatory T cells in transplantation and autoimmunity: recent progress and future directions. J. Mol. Cell Biol. *4*, 48–58.

Kashem, S.W., Haniffa, M., and Kaplan, D.H. (2017). Antigen-presenting cells in the skin. Annu. Rev. Immunol. *35*, 469–499.

Kim, N., Bae, K.B., Kim, M.O., Yu, D.H., Kim, H.J., Yuh, H.S., Ji, Y.R., Park, S.J., Kim, S., Son, K.-H., et al. (2012). Overexpression of cathepsin S induces chronic atopic dermatitis in mice. J. Invest. Dermatol. *132*, 1169–1176.

Kim, H.-J., Barnitz, R.A., Kreslavsky, T., Brown, F.D., Moffett, H., Lemieux, M.E., Kaygusuz, Y., Meissner, T., Holderried, T.A.W., Chan, S., et al. (2015). Stable inhibitory activity of regulatory T cells requires the transcription factor Helios. Science *350*, 334–339.

Li, Y., Qi, X., Liu, B., and Huang, H. (2015). The STAT5-GATA2 pathway is critical in basophil and mast cell differentiation and maintenance. J. Immunol. *194*, 4328–4338.

Liu, B., Tai, Y., Liu, B., Caceres, A.I., Yin, C., and Jordt, S.-E. (2019). Transcriptome profiling reveals Th2 bias and identifies endogenous itch mediators in poison ivy contact dermatitis. JCI Insight *5*, e124497.

Liu, Y., Lightfoot, Y.L., Seto, N., Carmona-Rivera, C., Moore, E., Goel, R., O'Neil, L., Mistry, P., Hoffmann, V., Mondal, S., et al. (2018). Peptidylarginine deiminases 2 and 4 modulate innate and adaptive immune responses in TLR-7–dependent lupus. JCI Insight *3*, e124729.

Ma, D.Y., and Clark, E.A. (2009). The role of CD40 and CD154/CD40L in dendritic cells. Semin. Immunol. *21*, 265–272.

Mack, M., Cihak, J., Simonis, C., Luckow, B., Proudfoot, A.E., Plachý, J., Brühl, H., Frink, M., Anders, H.J., Vielhauer, V., et al. (2001). Expression and characterization of the chemokine receptors CCR2 and CCR5 in mice. J. Immunol. *166*, 4697–4704.

Mahajan, S., Hogan, J.K., Shlyakhter, D., Oh, L., Salituro, F.G., Farmer, L., and Hoock, T.C. (2015). VX-509 (decernotinib) is a potent and selective janus kinase 3 inhibitor that attenuates inflammation in animal models of autoimmune disease. J. Pharmacol. Exp. Ther. *353*, 405–414.

Malhotra, N., Leyva-Castillo, J.M., Jadhav, U., Barreiro, O., Kam, C., O'Neill, N.K., Meylan, F., Chambon, P., Siegel, R.M., Wang, E.C., et al. (2018). RORα-expressing T regulatory cells restrain allergic skin inflammation. Sci. Immunol. *13*, eaao6923.

Man, M.-Q., Hatano, Y., Lee, S.H., Man, M., Chang, S., Feingold, K.R., Leung, D.Y.M., Holleran, W., Uchida, Y., and Elias, P.M. (2008). Characterization of a hapten-induced, murine model with multiple features of atopic dermatitis: structural, immunologic, and biochemical changes following single versus multiple oxazolone challenges. J. Invest. Dermatol. *128*, 79–86.

Mashiko, S., Mehta, H., Bissonnette, R., and Sarfati, M. (2017). Increased frequencies of basophils, type 2 innate lymphoid cells and Th2 cells in skin of patients with atopic dermatitis but not psoriasis. J. Dermatol. Sci. *88*, 167–174.

Mouly, E., Chemin, K., Nguyen, H.V., Chopin, M., Mesnard, L., Leite-de-Moraes, M., Burlen-defranoux, O., Bandeira, A., and Bories, J.-C. (2010). The Ets-1 transcription factor controls the development and function of natural regulatory T cells. J. Exp. Med. *207*, 2113–2125.

O'Brien, R.L., and Born, W.K. (2015). Dermal γδ T cells–What have we learned? Cell. Immunol. *296*, 62–69.

Oka, T., Sugaya, M., Takahashi, N., Takahashi, T., Shibata, S., Miyagaki, T., Asano, Y., and Sato, S. (2017). CXCL17 attenuates imiquimod-induced psoriasis-like skin inflammation by recruiting myeloid-derived suppressor cells and regulatory T cells. J. Immunol. *198*, 3897–3908.

Okoye, I.S., Houghton, M., Tyrrell, L., Barakat, K., and Elahi, S. (2017). Coinhibitory receptor expression and immune checkpoint blockade: maintaining a balance in CD8+ T cell responses to chronic viral infections and cancer. Front. Immunol. *8*, 1215.

Pantelyushin, S., Haak, S., Ingold, B., Kulig, P., Heppner, F.L., Navarini, A.A., and Becher, B. (2012). Rorγt+ innate lymphocytes and γδ T cells initiate psoriasiform plaque formation in mice. J. Clin. Invest. *122*, 2252–2256.

Park, J., Shrestha, R., Qiu, C., Kondo, A., Huang, S., Werth, M., Li, M., Barasch, J., and Suszták, K. (2018). Single-cell transcriptomics of the mouse kidney reveals potential cellular targets of kidney disease. Science *360*, 758–763.

Riol-Blanco, L., Sánchez-Sánchez, N., Torres, A., Tejedor, A., Narumiya, S., Corbí, A.L., Sánchez-Mateos, P., and Rodríguez-Fernández, J.L. (2005). The chemokine receptor CCR7 activates in dendritic cells two signaling modules that independently regulate chemotaxis and migratory speed. J. Immunol. *174*, 4070–4080.

Rosser, E., and Mauri, C. (2015). Regulatory B cells: origin, phenotype, and function. Immunity *42*, 607–612.

Rőszer, T. (2015). Understanding the mysterious M2 macrophage through activation markers and effector mechanisms. Mediators Inflamm. *2015*, 816460.

Schönefuss, A., Wendt, W., Schattling, B., Schulten, R., Hoffmann, K., Stuecker, M., Tigges, C., Lübbert, H., and Stichel, C. (2010). Upregulation of cathepsin S in psoriatic keratinocytes. Exp. Dermatol. *19*, e80–e88.

Siracusa, M.C., Kim, B.S., Spergel, J.M., and Artis, D. (2013). Basophils and allergic inflammation. J. Allergy Clin. Immunol. *132*, 788–789.

Sonnenberg, G.F., and Artis, D. (2015). Innate lymphoid cells in the initiation, regulation and resolution of inflammation. Nat. Med. *21*, 698–708.

Stoeckius, M., Hafemeister, C., Stephenson, W., Houck-Loomis, B., Chattopadhyay, P.K., Swerdlow, H., Satija, R., and Smibert, P. (2017).

Simultaneous epitope and transcriptome measurement in single cells. Nat. Methods *14*, 865–868.

Street, K., Risso, D., Fletcher, R.B., Das, D., Ngai, J., Yosef, N., Purdom, E., and Dudoit, S. (2018). Slingshot: cell lineage and pseudotime inference for single-cell transcriptomics. BMC Genomics *19*, 477.

Stuart, T., Butler, A., Hoffman, P., Hafemeister, C., Papalexi, E., Mauck, W.M., Hao, Y., Stoeckius, M., Smibert, P., and Satija, R. (2019). Comprehensive integration of single-cell data. Cell *177*, 1888–1902.e21.

Takekoshi, T., Tada, Y., Watanabe, T., Sugaya, M., Hoashi, T., Komine, M., Kawashima, T., Shimizu, T., Hau, C.S., Asahina, A., et al. (2010). Identification of a novel marker for dendritic cell maturation, mouse transmembrane protein 123. J. Biol. Chem. *285*, 31876–31884.

Tan, L., Sandrock, I., Odak, I., Aizenbud, Y., Wilharm, A., Barros-Martins, J., Tabib, Y., Borchers, A., Amado, T., Gangoda, L., et al. (2019). Single-cell transcriptomics identifies the adaptation of Scart1+ Vγ6+ T cells to skin residency as activated effector cells. Cell Rep. *27*, 3657–3671.e4.

Thomson, J.A., Troutt, A.B., and Kelso, A. (1993). Contact sensitization to oxazolone: involvement of both interferon-gamma and interleukin-4 in oxazolone-specific Ig and T-cell responses. Immunology *78*, 185–192.

Turchinovich, G., and Pennington, D.J. (2011). T cell receptor signalling in γδ cell development: strength isn't everything. Trends Immunol. *32*, 567–573.

Versteven, M., Van den Bergh, J.M.J., Marcq, E., Smits, E.L.J., Van Tendeloo, V.F.I., Hobo, W., and Lion, E. (2018). Dendritic cells and programmed death-1 blockade: a joint venture to combat cancer. Front. Immunol. *9*, 394.

Villani, A.-C., Satija, R., Reynolds, G., Sarkizova, S., Shekhar, K., Fletcher, J., Griesbeck, M., Butler, A., Zheng, S., Lazo, S., et al. (2017). Single-cell RNA-seq reveals new types of human blood dendritic cells, monocytes, and progenitors. Science *356*, eaah4573.

Viola, A., and Luster, A.D. (2008). Chemokines and their receptors: drug targets in immunity and inflammation. Annu. Rev. Pharmacol. Toxicol. *48*, 171–197.

Vivier, E., Artis, D., Colonna, M., Diefenbach, A., Santo, J.P.D., Eberl, G., Koyasu, S., Locksley, R.M., McKenzie, A.N.J., Mebius, R.E., et al. (2018). Innate lymphoid cells: 10 years on. Cell *174*, 1054–1066.

Vocanson, M., Hennino, A., Rozières, A., Poyet, G., and Nicolas, J.-F. (2009). Effector and regulatory mechanisms in allergic contact dermatitis. Allergy *64*, 1699–1714.

Wang, B., Fujisawa, H., Zhuang, L., Freed, I., Howell, B.G., Shahid, S., Shivji, G.M., Mak, T.W., and Sauder, D.N. (2000). CD4+ Th1 and CD8+ type 1 cytotoxic T cells both play a crucial role in the full development of contact hypersensitivity. J. Immunol. *165*, 6783–6790.

Weber, F.C., Németh, T., Csepregi, J.Z., Dudeck, A., Roers, A., Ozsvári, B., Oswald, E., Puskás, L.G., Jakob, T., Mócsai, A., et al. (2015). Neutrophils are required for both the sensitization and elicitation phase of contact hypersensitivity. J. Exp. Med. *212*, 15–22.

Wenzel, J., Uerlich, M., Haller, O., Bieber, T., and Tueting, T. (2005). Enhanced type I interferon signaling and recruitment of chemokine receptor CXCR3-expressing lymphocytes into the skin following treatment with the TLR7-agonist imiquimod. J. Cutan. Pathol. *32*, 257–262.

Yamakita, Y., Matsumura, F., Lipscomb, M.W., Chou, P., Werlen, G., Burkhardt, J.K., and Yamashiro, S. (2011). Fascin1 promotes cell migration of mature dendritic cells. J. Immunol. *186*, 2850–2859.

Yu, Y.-R.A., O'Koren, E.G., Hotten, D.F., Kan, M.J., Kopin, D., Nelson, E.R., Que, L., and Gunn, M.D. (2016). A protocol for the comprehensive flow cytometric analysis of immune cells in normal and inflamed murine non-lymphoid tissues. PLoS One *11*, e0150606.

Zhang, S., Leistico, J.R., Cook, C., Liu, Y., Cho, R.J., Cheng, J.B., and Song, J.S. (2020). Riemannian geometry and statistical modeling correct for batch effects and control false discoveries in single-cell surface protein count data. Phys. Rev. E *102*, 012409.

Zheng, Y., Danilenko, D.M., Valdez, P., Kasman, I., Eastham-Anderson, J., Wu, J., and Ouyang, W. (2007). Interleukin-22, a T(H)17 cytokine, mediates IL-23-induced dermal inflammation and acanthosis. Nature *445*, 648–651.

iScience, Volume *23*

Supplemental Information

Single-Cell Profiling Reveals Divergent, Globally Patterned Immune Responses in Murine Skin Inflammation

Yale Liu, Christopher Cook, Andrew J. Sedgewick, Shuyi Zhang, Marlys S. Fassett, Roberto R. Ricardo-Gonzalez, Paymann Harirchian, Sakeen W. Kashem, Sho Hanakawa, Jacob R. Leistico, Jeffrey P. North, Mark A. Taylor, Wei Zhang, Mao-Qiang Man, Alexandra Charruyer, Nadejda Beliakova-Bethell, Stephen C. Benz, Ruby Ghadially, Theodora M. Mauro, Daniel H. Kaplan, Kenji Kabashima, Jaehyuk Choi, Jun S. Song, Raymond J. Cho, and Jeffrey B. Cheng

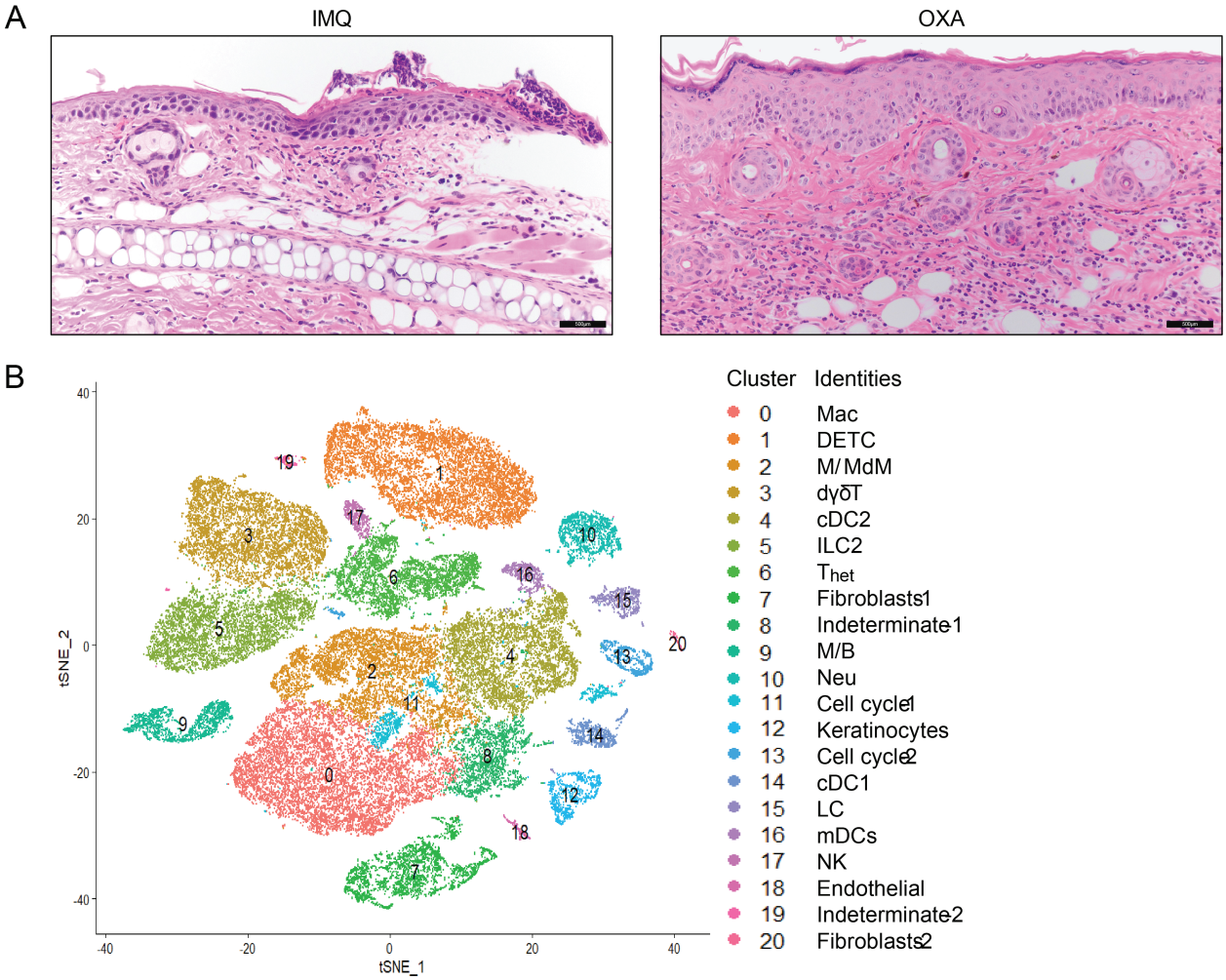

Figure S1. Histology and cell types with imiquimod-and oxazolone-induced skin inflammation (related to Figure 1 and Table S5). (A) Representative hematoxylin and eosin-stained histological sections of imiquimod-treated (left, 200x) and oxazolone-treated (right, 200x) mouse ear skin, at time of harvesting for single cell isolation. Scale bar 500 microns. (B) t-SNE plot shows initial 21 clusters conserved across treatment conditions, delineated by Louvain clustering. Each dot represents one of 52,086 profiled cells.

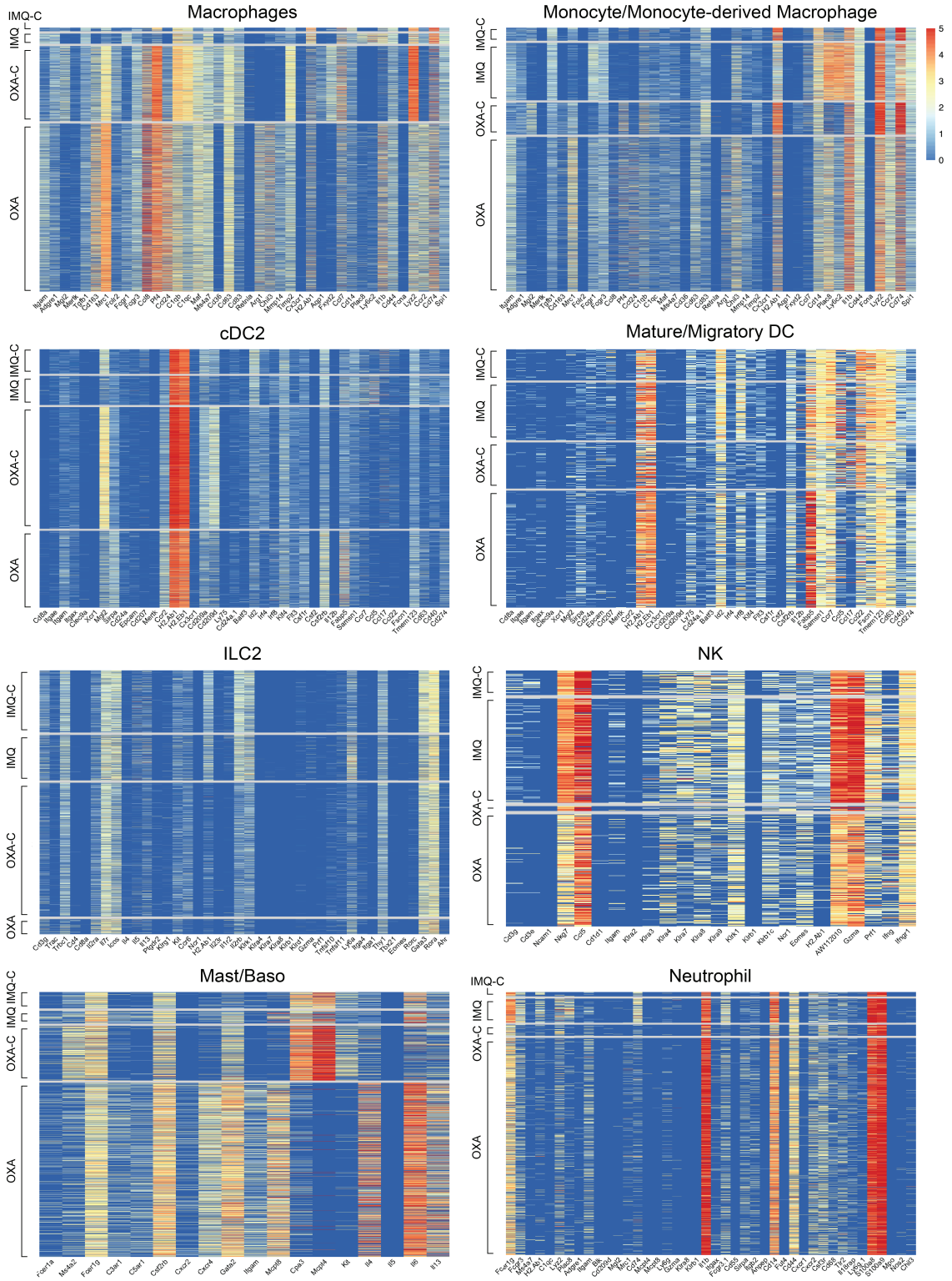

Figure S2. Cluster-specific heatmaps with selected marker genes (related to Figure 2, Table S2, and Table S3). Normalized RNA expression count values of selected marker genes on the x-axis and single cells on the y-axis. Cells are ordered on y-axis by treatment condition (IMQ-C, IMQ, OXA-C, OXA).

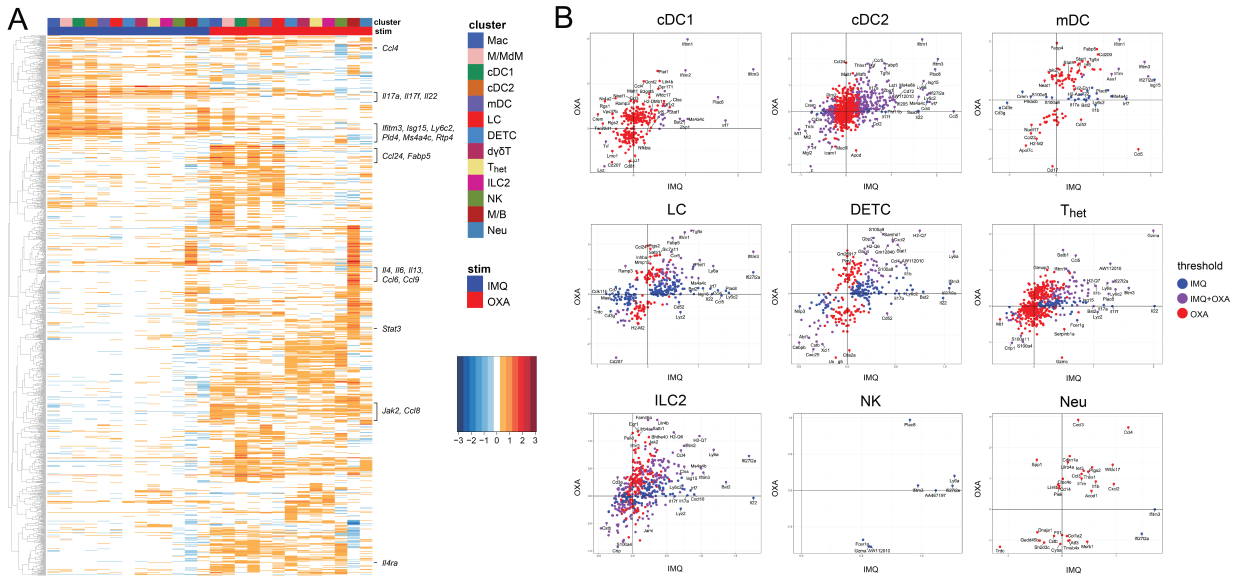

Figure S3. Divergent immune cell transcriptomes with imiquimod- and oxazolone- induced skin inflammation (related to Figure 3, Table S4, and Table S5). (A) Unsupervised hierarchical clustering heatmap for treatment-induced differentially expressed genes on a per cluster basis. Columns depict average logFC of oxazolone or imiquimod treated cells (vs control) for each cluster. Rows depict 885 treatment-specific DEGs with average log fold change > 0.5 and p.adj < 0.05 in at least one cluster for either treatment arm (OXA vs. OXA-C and IMQ vs. IMQ-C). (B) Cluster-specific scatter plots showing OXA or IMQ treatment-induced differentially expressed genes for cDC1, cDC2, mDC, LC, DETC, T_{het}, ILC2, NK, and Neu populations (avg_logFC for IMQ DEGs relative to IMQ-C on x-axis and OXA DEGs relative to OXA-C on y-axis). Pseudocolored dots represent significant DEGs (p.adj < 0.05) for OXA (red), IMQ (blue), or both treatments (purple).

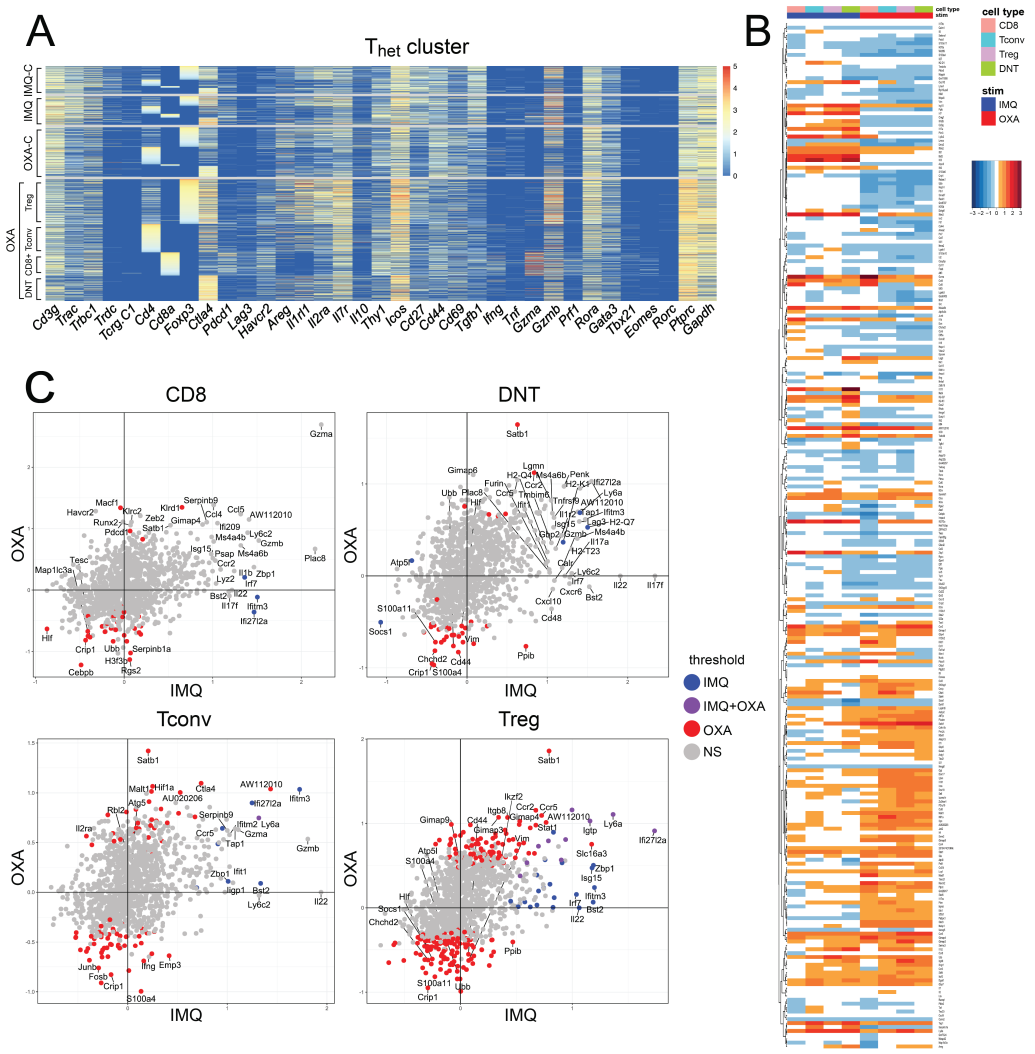

Figure S4. **Imiquimod and oxazolone divergently reprogram T cell subpopulations (related to Figure 3, Table S2, and Table S4).** (A) Single-cell heatmap for the T_{het} cluster displaying normalized RNA expression count values of selected marker genes on the x-axis and single cells on the y-axis. Cells were grouped by treatment condition and then ordered along the y-axis sequentially by expression of key T-cell marker genes (*Foxp3* → *Cd4* → *Cd8a* → *Ctla4)* to reveal subpopulations. (B) Unsupervised hierarchical clustering heatmap of treatment-induced differentially expressed genes for the 4 T cell subpopulations. Columns depict average logFC of oxazolone or imiquimod treated cells (vs control) for each T-cell subpopulation, for each treatment condition. Rows depict 265 treatment-specific genes composed of DEGs with average log fold change > 0.5 and p.adj < 0.05 in at least one population for either each treatment arm (OXA vs. OXA-C and IMQ vs. IMQ-C) and a manually curated list of type I/type II/type 17/interferon response genes and T-cell co-inhibitory receptors. (C) Scatter plots showing DEGs for OXA or IMQ for $CD8^+$ T cells, Conventional $CD4^+$ T cells (Tconv), $Foxp3^+$ Tregs, and double negative regulatory T cell (DNT) populations (IMQ DEGs relative to IMQ-C on x-axis and OXA DEGs relative to OXA-C on y-axis). Pseudocolored dots represent significant DEGs (p adj value < 0.05) for OXA (red), IMQ (blue), or both treatments (purple). Genes in grey did not reach statistical significance in either OXA or IMQ treatment arms.

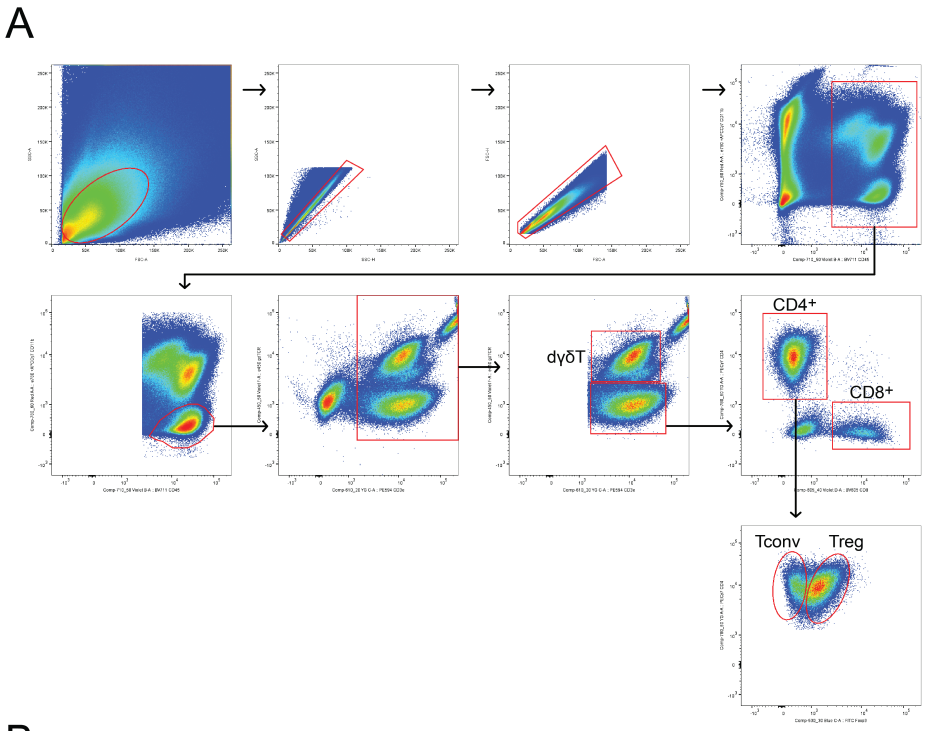
A
dγδT
CD4+
CD8+
Tconv
Treg
B
dγδT
Tconv
CD8+
Treg
IL-17A
IL-22
CCL5
% of CD3+ T cells
IMQ-C
IMQ
C
IMQ-C
IMQ

Figure S5. Intracellular cytokine flow cytometry analysis of imiquimod-treated cutaneous immune populations (related to Figure 3 and Table S4). (A) Gating strategy and sub-population identification of isolated cutaneous immune cells from IMQ and IMQ-C treated mice. PMA and ionomycin-stimulated cells were stained for cell markers (CD45, CD3, CD4, CD8, γδTCR, CD11b, FOXP3) and intracellular cytokines/chemokines (IL17A, IL22, and CCL5). Concatenated flow plots of 5 imiquimod treated samples are depicted. (B) Bar graphs depict frequency of cytokine/chemokine-expressing cutaneous immune populations with IMQ and IMQ-C treatment (5 mice per condition; *t* test, unpaired, two-tailed, * $P < 0.05$, ** $P < 0.01$, *** $P < 0.001$; Data are reported as mean ± SEM) (C) Representative intracellular staining plots from each population in A used to assess the frequency of cytokine/chemokine expression in IMQ treated cells.

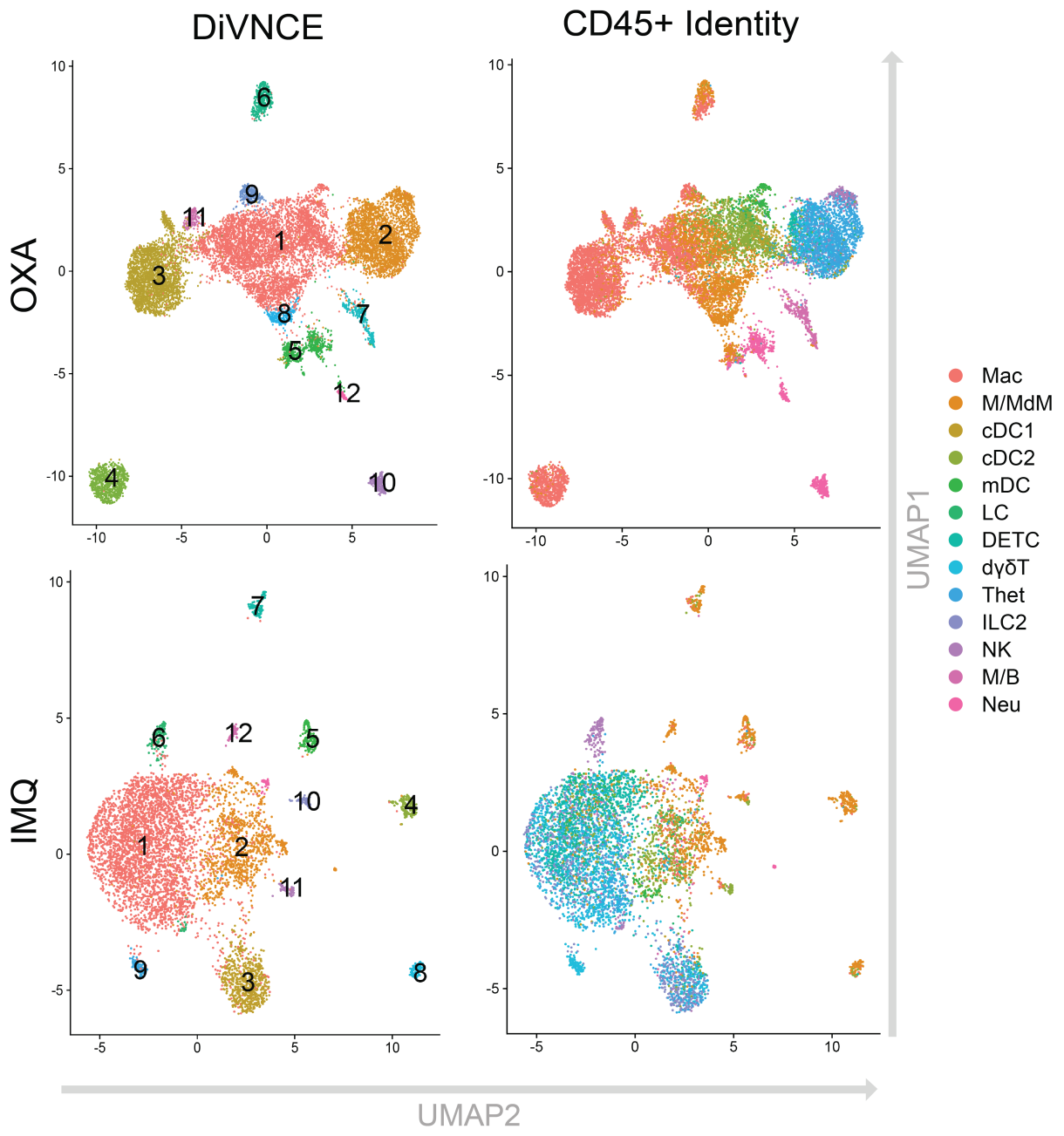

Figure S6. DiVNCE cluster representations with mapping to Table S6 (related to Figure 5 and Table S6). UMAP representation showing partitioning of oxazolone treated cells based on 12 DiVNCE profiles (upper left panel), with same clusters colored by cell identities as depicted in Fig 1A (upper right). Lower left panel shows imiquimod treated cells partitioned on 12 DiVNCE profiles and same clusters colored by cell identity (lower right). DiVNCE numbering in left panels corresponds to DiVNCE cluster numbering in Table S6.

KEY RESOURCES TABLE

REAGENT or RESOURCE	SOURCE	IDENTIFIER
Antibodies		
CD16/CD32 Fc Block	BD biosciences	Cat#BDB553141
CD16/CD32 Fc Block	BioXCell	Cat#BE0307
anti-CD45-APC-Cy7	BD Biosciences	Cat#30F-11
anti-CD45-APC	BD Biosciences	Cat#17-0451-82
TotalSeq™-A anti-mouse CD3	Biolegend	Cat#100251
TotalSeq™-A anti-mouse CD4	Biolegend	Cat#100569
TotalSeq™-A anti-mouse CD8a	Biolegend	Cat#100773
TotalSeq™-A anti-mouse CD69	Biolegend	Cat#104546
TotalSeq™-A anti-mouse CD62L	Biolegend	Cat#104451
TotalSeq™-A anti-mouse CD44	Biolegend	Cat#103045
TotalSeq™-A anti-mouse CD25	Biolegend	Cat#102055
TotalSeq™-A anti-mouse CD127 (IL-7Rα)	Biolegend	Cat#135045
TotalSeq™-A anti-mouse TCR γ/δ	Biolegend	Cat#118137
TotalSeq™-A anti-mouse CD19	Biolegend	Cat#115559
TotalSeq™-A anti-mouse IgM	Biolegend	Cat#406535
TotalSeq™-A anti-mouse CD335 (NKp46)	Biolegend	Cat#137633
TotalSeq™-A anti-mouse NK-1.1	Biolegend	Cat#108755
TotalSeq™-A anti-mouse CD90.2	Biolegend	Cat#105345
TotalSeq™-A anti-mouse I-A/I-E	Biolegend	Cat#107653
TotalSeq™-A anti-mouse CD45R/B220	Biolegend	Cat#103263
TotalSeq™-A anti-mouse CD11b	Biolegend	Cat#101265
TotalSeq™-A anti-mouse CD172a (SIRPα)	Biolegend	Cat#144033

TotalSeq™-A anti-mouse XCR1	Biolegend	Cat#148227
TotalSeq™-A anti-mouse CD103	Biolegend	Cat#121437
TotalSeq™-A anti-mouse CD64 (FcγRI)	Biolegend	Cat#139325
TotalSeq™-A anti-mouse CD11c	Biolegend	Cat#117355
TotalSeq™-A anti-mouse CD24	Biolegend	Cat#101841
TotalSeq™-A anti-mouse CD326 (Ep-CAM)	Biolegend	Cat#118237
TotalSeq™-A anti-mouse CD195 (CCR5)	Biolegend	Cat#107019
TotalSeq™-A anti-mouse CD196 (CCR6)	Biolegend	Cat#129825
TotalSeq™-A anti-mouse CXCR4	Biolegend	Cat#146520
TotalSeq™-A anti-mouse CD134 (OX-40)	Biolegend	Cat#119426
TotalSeq™-A anti-mouse CD278 (ICOS)	Biolegend	Cat#313555
TotalSeq™-A anti-mouse CD223 (LAG-3)	Biolegend	Cat#125229
TotalSeq™-A anti-mouse CD274 (B7-H1, PD-L1)	Biolegend	Cat#153604
TotalSeq™-A anti-mouse KLRG1 (MAFA)	Biolegend	Cat#138431
TotalSeq™-A anti-mouse CD27	Biolegend	Cat#124235
TotalSeq™-A anti-mouse CD21/CD35 (CR2/CR1)	Biolegend	Cat#123427
TotalSeq™-A anti-mouse CD86	Biolegend	Cat#105047
TotalSeq™-A anti-mouse IgD	Biolegend	Cat#405745
TotalSeq™-A anti-mouse CD1d (CD1.1, Ly-38)	Biolegend	Cat#123529
TotalSeq™-A anti-mouse CD138 (Syndecan-1)	Biolegend	Cat#142532
TotalSeq™-A anti-mouse CD117 (c-kit)	Biolegend	Cat#105843
TotalSeq™-A anti-mouse CX3CR1	Biolegend	Cat#149041
TotalSeq™-A anti-mouse F4/80	Biolegend	Cat#123153
TotalSeq™-A anti-mouse CD192 (CCR2)	Biolegend	Cat#150625
CCL5	Biolegend	Cat#149103

CD3epsilon	Biolegend	Cat#50-7177-82
CD4	Biolegend	Cat#100421
gdTCR	Biolegend	Cat#118119
IL-22	Biolegend	Cat#516411
CD8alpha	Biolegend	Cat#100743
CD45	Biolegend	Cat#103147
CD11b	Biolegend	Cat#101225
Foxp3	eBioscience	Cat#11-5773-82
IL-17A	eBioscience	Cat#17-7177-81
Fixable viability stain eflour 780	Thermofisher	Cat#65-0865-14
Chemicals, Peptides, and Recombinant Proteins		
Imiquimod	Taro pharmaceuticals	Cat# 51672-4145-6
Vehicle (vanicream moisturizing cream)	Vanicream, Pharmaceutial Specialties, Inc.	N/A
Oxazolone	Sigma-Aldrich	Cat#E0753
Ethanol	Fisher Brand	Cat#HC-1000-1GL
RPMI 1640	UCSF Cell Culture Facility	Cat#CCFAE001
FBS	UCSF Cell Culture Facility	Cat#CCFAQ008
Liberase TL	Sigma	Cat# 5401020001
DNAse I	Sigma	Cat#10104159001
Collagenase XI	Sigma	Cat# c9407
DAPI (4′,6-diamidine-2′-phenylindole dihydrochloride)	Life Technologies	Cat#A20502
Human TruStain FcX	Biolegend	Cat#422301
Cell stain buffer	Biolegend	Cat#420201
Chromium Single cell 3’ Solution V2 kit	10x Genomics	Cat#220104
Chromium Single cell 3’ Solution V3 kit	10x Genomics	Cat#2000059
SPRI beads	Beckman Coulter	Cat#B23317
ADT additive primer	IDT	CCT TGG CAC CCG AGA ATT* C*C
SI PCR primer	IDT	AATGATACGGCGACCACCGAGATCTA CACTCTTTCCCTACACGACGC*T*C
TruSeq small RNA RPI1	IDT	CAAGCAGAAGACGGCATACGAGATC GTGATGTGACTGGAGTTCCTTGGCAC CCGAGAATTC*C*A

TruSeq small RNA RPI2	IDT	CAAGCAGAAGACGGCATACGAGATA CATCGGTGACTGGAGTTCCTTGGCAC CCGAGAATTC*C*A
TruSeq small RNA RPI3	IDT	CAAGCAGAAGACGGCATACGAGATG CCTAAGTGACTGGAGTTCCTTGGCAC CCGAGAATTC*C*A
TruSeq small RNA RPI4	IDT	CAAGCAGAAGACGGCATACGAGATT GGTCAGTGACTGGAGTTCCTTGGCAC CCGAGAATTC*C*A
TruSeq small RNA RPI5	IDT	CAAGCAGAAGACGGCATACGAGATC ACTGTGTGACTGGAGTTCCTTGGCAC CCGAGAATTC*C*A
TruSeq small RNA RPI6	IDT	CAAGCAGAAGACGGCATACGAGATAT TGGCGTGACTGGAGTTCCTTGGCAC CCGAGAATTC*C*A
Kapa library quantitation kit	Kapa Biosystems	Cat#KK2601
Deposited Data		
scRNA-seq and CITE-seq data from this publication		GSE149121
Experimental Models: Cell Lines		
HEK 293 cells	Sigma	Cat#85120602-1VL
Experimental Models: Organisms/Strains		
Mouse: C57BL/6J	Jackson Laboratory	Cat#: 000664
Software and Algorithms		
10x Cellranger v3.1.0	10x Genomics	https://support.10xgenomics.com/single-cell-gene-expression/software/downloads/latest?
Mouse (mm10) reference dataset	10x Genomics	https://support.10xgenomics.com/single-cell-gene-expression/software/downloads/latest?
Human (GRCh38) and mouse (mm10) reference dataset	10x Genomics	https://support.10xgenomics.com/single-cell-gene-expression/software/downloads/latest?
Seurat v3.1.2	Satija Lab	https://satijalab.org/seurat/install.html
Rstudio v1.2.5033	RStudio, Inc.	https://rstudio.com/
R v3.6.2	N/A	https://cran.r-project.org/mirrors.html
Slingshot 1.4.0	N/A	https://bioconductor.org/packages/release/bioc/html/slingshot.html

Table S1 scRNA-seq dataset metrics (related to Figure 1)

Samples	Estimated Number of Cells	Post-filtering # of cells	Mean Reads per Cell
IMQ-C1	3,584	3,339	157,072
IMQ-C2	2,641	2,280	214,772
IMQ-C3	4,022	3,626	160,432
IMQ1	3,426	3,376	138,165
IMQ2	1,728	1,685	323,814
IMQ3	2,739	2,411	212,937
OXA-C1	5,304	4,576	32,558
OXA-C2	6,875	6,075	26,164
OXA-C3	7,941	7,378	21,694
OXA1	8,123	6,923	22,311
OXA2	6,333	5,160	23,309
OXA3	6,860	5,257	23,291

Table S3 Representative marker genes for immune cell populations (related to Figure 1 and Figure 2)

	Classic markers	% cells in cluster	Adjusted p-value	Extended markers	% cells in cluster	Adjusted p-value	Negative markers
Macrophage (Mac)	*Adgre1*	41.4	2.9E-112	*Mrc1*	93.9	2.3E-81	
	Ms4a7	71.6	1.0E-249	*Folr2*	28.2	5.8E-103	
	C1qc	66.3	2.4E-222	*Arg1*	35.9	0	
	Itgam	47.1	4E-160	*Chil3*	32.6	0	
	Cd68	63.3	1.5E-58				
Monocytes/Monocyte-derived Macrophages (M/MdM)	*Adgre1*	34.8	4E-273				
	Itgam	61.6	1.1E-157				
	Fcgr1	49.3	1.1E-82				
	Cd14	67.9	5.4E-16				
	Plac8	67.5	0				
	Ly6c2	51.3	7.1E-176				
	Lyz2	88.4	3.1E-216				
Type 1 conventional dendritic cells (cDC1)	*H2-Ab1*	100	2.9E-58				
	H2-Eb1	99.9	7.5E-59				
	Clec9a	36.7	0				
	Xcr1	30.0	7.1E-171				
	Irf8	91.8	9.2E-63				
	Batf3	46.5	1.3E-40				
Type 2 conventional dendritic cells (cDC2)	*H2-Aa*	97.9	1.3E-267				
	H2-Eb1	97.4	1.7E-271				
	Itgax	21.5	6.6E-68				
	Mgl2	70.6	2.3E-246				
	Cd209a	58.2	0				
	Cd209d	58.0	1.7E-239				
	Sirpa	55.1	0				
	Irf4	28.5	0				
Mature/Migratory Dendritic cells (mDC)	*Fscn1*	80.2	0				
	Cacnb3	82.3	0				
	Ccr7	89.5	5.7E-141				
	Cd40	60.4	5.6E-96				
	Tmem123	97.5	6.7E-29				
	Cd274	67.8	1.4E-18				
Langerhans Cells (LC)	*H2-Eb1*	99.9	1.2E-53				
	H2-Ab1	99.9	6.5E-52				
	Cd207	91.8	1E-290				
	Epcam	87.4	1.2E-167				
	Cd24a	70.2	4.3E-23				
	Csf1r	89.0	1.6E-07				
Dendritic Epidermal T cells (DETC)	*Cd3e*	94.6	3.9E-87				*Cd4*
	Cd3g	98.4	2.1E-202				*Cd8a*
	Trdc	98.7	0				
	Tcrg-C1	89.8	0				
	Thy1	79.4	3.9E-94				
Dermal gamma delta T cells (dγδT)	*Cd3g*	90.0	2.3E-37				
	Trdc	76.5	5.2E-25				
	Tcrg-C1	43.5	0	*5830411 N06Rik*	54.6	0	*Cd4*
	Tcrg-C2	22.74	0				
	Tcrg-C4	9.31	1.2E-22	*Cd163l1*	36.0	3.3E-181	*Cd8a*
	Thy1	71.0	1.2E-69				
	Cd44	78.4	1.9E-90				
	Cd69	51.3	1.5E-40				
Heterogeneous T cells (T^{het})	*Cd3d*	60.6	2.6E-13				
	Trac	41.1	5.1E-156				

	Trbc1	41.2	1.7E-147				
	Trbc2	60.1	9.3E-129				
	Cd4	23.5	9.8E-140				
	Cd8a	8.4	--				
	Foxp3	23.7	1.3E-109				
Type 2 Innate lymphoid cells (IIC2)	*Gata3*	73.0	1.5E-252				*Cd3d/e/g*
	Rora	84.9	2.5E-224				*Eomes*
	Il7r	77.4	2.1E-75				*Rorc*
	Il5	12.0	0				*Tbx21*
	Il13	20.4	1.3E-225				*Cd4*
Natural Killer Cells (NK)	*Gzma*	95.7	0				
	Klra8	50.1	0				
	Klra7	41.1	5.9E-144				
	Klrb1c	56.2	2E-184				
	Eomes	50.7	0				
	Ncr1	36.2	0				
	Prf1	67.7	0				
Mast cells/basophils (M/B)				*Kit*	15.5	2.6E-170	
	Gata2	71.2	6.6E-258	*Mcpt4*	28.4	0	
	Ms4a2	31.1	0	*Itgam*	26.7	3.8E-49	
				Mcpt8	51.8	0	
Neutrophils (Neu)	*S100a8*	97.4	3.1E-141				
	S100a9	98.0	5.6E-182				
	Csf3r	43.2	1.4E-25				
	Cebpd	11.6	1.1E-74				
	Slc11a1	21.0	0				
	Spi1	24.1	8E-130				

Note:

Markers with adjusted p-value in black text are output from table 2 (FindConservedMarkers output) and in red text are output from table 2 (FindAllMarkers output). The FindConservedMarkers function identifies differentially expressed genes between clusters that are conserved across all treatment conditions. For marker genes that are enriched in a given cluster but are only upregulated in specific treatment conditions (e.g. *Arg1*, *Chil3* representing the increase in tissue-remodelling macrophages with OXA treatment or *Mcpt8* in the M/B cluster representing the basophil influx in OXA-treated immune cells), these DEGs would be missed by FindConservedMarkers. Thus, we also ran the FindAllMarkers function which performs differential expression analysis for all cells in a cluster (irrespective of treatment condition) against cells from all other clusters.

Table S5 Relative percentages of immune cell populations for each treatment condition (related to Figure 3)

Cluster	% of all IMQ-C cells	% of all IMQ cells	% of all OXA-C cells	% of all OXA cells
Mac	1.31	4.90	16.42	33.26
M/MdM	3.27	18.87	4.79	21.09
cDC1	1.52	1.65	2.22	1.09
cDC2	5.62	8.71	17.27	9.88
LC	2.73	3.07	1.23	0.43
mDC	0.80	1.98	0.73	1.71
DETC	47.95	15.45	14.01	1.11
dγδT	15.55	17.96	17.25	2.25
Thet	6.68	8.87	7.04	12.03
ILC2	12.43	11.95	16.31	1.68
NK	0.64	3.46	0.07	1.54
M/B	1.19	1.15	2.24	6.61
Neu	0.30	1.98	0.42	7.32

Thet subpopulations	% of all IMQ-C cells	% of all IMQ cells	% of all OXA-C cells	% of all OXA cells
CD8+	0.42	0.77	0.27	2.03
CD4+	0.72	1.23	1.17	1.74
Treg	1.59	1.46	1.37	2.56
DNT	0.64	0.95	0.66	1.25

Transparent Methods

Mice treatment

Mouse experiments were conducted according to protocols approved by the Institutional Animal Care Use Committees at UCSF and the San Francisco Veteran's Affairs Medical Center, following the recommendations of the American Association for the Accreditation of Laboratory Animal Care. Male C57BL/6J mice were purchased from the Jackson Laboratory and housed in specific pathogen-free conditions and treated at 8 weeks of age.

IMQ-induced skin inflammation was performed as previously described (Gray et al., 2013). Briefly, three mice received a daily topical thin coat of commercially available IMQ cream (5%) (Taro pharmaceuticals) on both ears for 7 consecutive days. Control mice were treated similarly with vehicle cream (Vanicream Moisturizing Skin Cream, Pharmaceutical Specialties, Inc.). Mouse ear skin samples were collected 24h after the last application.

Oxazolone (OXA; Sigma-Aldrich)-induced skin inflammation was performed as previously described (Man et al., 2008). OXA and control treated mice were sensitized by applying two 50uL treatments of 3% OXA in ethyl alcohol (EtOH) on shaved dorsal skin 24h apart. Nine days after sensitization, OXA treated mice were challenged with 10ul of 0.5% OXA in EtOH to the dorsal and ventral pinnae of both ears (40uL total per mouse) every other day for 3 challenges, while control mice were treated with 100% EtOH. Mouse ear skin samples were collected 24 hours following the final challenge.

Cutaneous immune cell isolation

Mouse ears were minced and incubated in digestion media A (5 ml of RPMI 1640 supplemented with 10% FBS, 100uL of a 12.5 mg/ml stock of Liberase TL (Sigma 5401020001), and 50uL 0.1mg/ml of DNAse I (Sigma 10104159001)) for IMQ/IMQ-C samples or digestion buffer B (RPMI 1640 supplemented with 10% FBS, collagenase XI (2 mg/mL; Sigma c9407), and DNAse I (0.1 mg/mL; Sigma 10104159001) for OXA/OXA-C samples at 37 °C for 90 minutes with 200–250 rpm agitation. Cells were dispersed using a tissue dissociator (GentleMACS; Miltenyi Biotec – running program C) for 44s. Single cell suspensions were passed through 40-100 µm filters and washed with FACS buffer (PBS with 2% FBS). Isolated cutaneous cells were incubated at 4 °C with blocking buffer composed of 20 uL mouse CD16/CD32 FcBlock (BD biosciences, #553141) for

OXA/OXA-C or 10uL of 1mg/ml stock of Fc Block (Bioxcell, #BE0307) for IMQ/IMQ-C diluted into 1 mL FACS buffer for 15 minutes.

This was followed by addition of a 1:200 dilution of mouse CD45 antibody conjugated to APC-Cy7 (BD Biosciences, 30F-11) for IMQ single cell suspensions and a 1:40 dilution of mouse CD45 antibody conjugated to APC fluorophore (BD Biosciences, #17-0451-82) for OXA single cell suspensions for 30 minutes. Live/dead exclusion was performed using 0.1 mg/mL DAPI (4′,6-diamidino-2′-phenylindole dihydrochloride) and CD45 positive cells were collected by flow cytometry cell sorting using a MoFlo Cell Sorter (Beckman Coulter) or a SH800S Cell Sorter (Sony Biotechnology) for IMQ and OXA samples, respectively. IMQ sorted cells were then centrifuged and resuspended in PBS with 0.04% FBS. OXA/OXA-C single cell suspensions were spiked with 5% HEK 293 cells and incubated with blocking solution for CITE-seq (93 uL cell stain buffer (Biolegend, #420201), 5 uL Human TruStain FcX (Biolegend, Cat#422301), and 2 uL Mouse Fc block (BD biosciences, #553141) at 4 °C for 10 minutes, and then with 0.5 ug/1 million cells of TotalSeq™-A antibodies (Biolegend) for 30 minutes at 4 °C. OXA/OXA-C cells were then washed with cell staining buffer three times and resuspended in 10ul cell staining buffer (Biolegend, #420201).

Single cell RNA and Cellular Indexing of Transcriptomes and Epitopes by Sequencing (scRNA- and CITE-seq)

Single cell Gel-bead-in-Emulsions and mRNA libraries were generated by the Genomics Core Facility, UCSF Institute for Human Genetics per manufacturer's protocol (Chromium Single cell 3' Solution V2 kit for IMQ samples and V3 kit for OXA samples; 10x Genomics, Pleasanton, CA) except for the addition of 1 µl ADT(antibody derived tag) additive primer at the cDNA amplification step for OXA samples. For OXA samples, CITE-seq libraries were prepared according to TotalSeq-A Antibodies with 10x Single Cell 3' Reagent Kit v3 3.1 manufacturer's protocol (Biolegend) with slight modifications. In brief, ADTs (cDNA amplification supernatant) were purified with 2 rounds of 2X SPRI beads and then amplified for fourteen cycles using HiFi HotStart ReadyMix (2X) (KAPA, Roche Sequencing & Life Science, Wilmington, MA) and 2.5 uM of oligos corresponding to SI PCR primer and Truseq Small RNA RPI1-6 primers. After amplification, libraries were purified by 1.2X SPRI bead cleanup, and then QC and quantification performed with Agilent 2100 Tape station and Kapa library quantitation kit prior to sequencing. mRNA and ADT libraries were sequenced using an Illumina Novaseq 6000 (IMQ/IMQ-C) or HiSeq 4000 (OXA/OXA-C) per manufacturer's instructions. Sequencing parameters for the Novaseq 6000

were read 1, 26 cycles; i7 index, 8 cycles; i5 index, 0 cycles; and read 2, 98 cycles, while Paired end 150 base pair sequencing was used on the HiSeq 4000.

Single-cell data pre-processing and QC

FASTQ files were initially processed using Cellranger version 3.1.0 to perform sample de-multiplexing, barcode processing, single-cell gene UMI-counting, and feature barcode (CITE-Seq) read-matching. IMQ/IMQ-C transcripts were mapped to the mm10 reference genome while OXA/OXA-C transcripts were mapped to the mm10 + GRCh38 reference genome (as OXA/OXA-C samples contained spike-in human cells to assess for CITE-seq background staining levels). Data from ambient RNA was trimmed based on an UMI-barcode saturation curve. Post-quality control, 41,436 cells were obtained from the OXA experiment (21,316 cells from OXA-treated mice and 20,120 cells from OXA-C mice), and 17,870 cells were obtained from the Imiquimod experiment (7,623 cells from IMQ-stimulated mice and 10,247 cells from IMQ-C) (Table S1).

Data were further filtered using the Seurat package (version 3.1.2) in R (version 3.6.1). Cells were filtered to include only cells displaying > 300 genes/cell and < 4000 genes/cell, and no more than 20% mitochondrial gene expression. Post-filtration we obtained 52,086 cells in total, 35,369 were obtained from the OXA experiment (17,340 cells from OXA-treated mice and 18,029 cells from OXA-C mice), and 16,717 cells were obtained from the IMQ experiment (7,427 cells from IMQ-stimulated mice and 9,245 cells from controls) (Table S1).

Seurat integration with batch correction

In our analysis, we used Seurat v3.1.2 in Rstudio to perform batch-effect correction. Log-normalization was first used to normalize datasets with NormalizeData function and 3000 highly variable genes were defined within the twelve mouse samples with the Seurat FindVariableFeatures function. We also identified unsupervised integration "anchors" for similar cell states using shared nearest neighbor graphs (FindIntegrationAnchors), and then integrated (IntegrateData function) our 4 different treatment datasets using these anchors. The output was then transformed into principal component analysis (PCA) space for further evaluation and visualization.

ScRNA-seq clustering

To identify cell clusters, PCA was first performed on the list of highly variable genes. Significant PCs were identified using an Elbowplot and the first 30 PCs were used for clustering with the

Louvain modularity-based community detection algorithm (Stuart et al., 2019) to generate cell clusters (FindClusters function, 21 clusters with resolution = 0.35). To present high dimensional data in two-dimensional space, we performed t-SNE analysis using the results of PCA with significant PCs as input. Cluster-specific marker genes were found using the Seurat functions FindConservedMarkers and FindAllMarkers using the Model-based Analysis of Single-cell Transcriptomics (MAST) test (Finak et al., 2015; Luecken and Theis, 2019). Cell types for each cluster were determined using marker genes collated from the literature. This analysis identified 21 total clusters (Figure S2), for which we excluded non-immune clusters (cluster 7, 12, 18), clusters enriched for cell cycle genes (cluster 11, 13, 20), and two other small $CD45^+$ groupings (cluster 8, 19) with indeterminate identity and/or obvious heterogeneity.

Identification of treatment-induced differentially expressed genes

Treatment-induced (OXA vs OXA-C and IMQ vs IMQ-C) differentially expressed genes (DEGs) were identified for each cluster using the FindMarkers function from the Seurat R package using MAST. Genes were considered differentially expressed if they had an average log fold-change of more than 0.25 and the p.adj was lower than 0.05. Treatment-induced differentially expressed genes were displayed on a scatterplot using the R package “ggplot2” for DEGs (p.adj< 0.05) from each cluster.

To identify putative T cell subtypes, first a single-cell heatmap of normalized RNA expression count values was constructed within the T_{het} cluster and sequentially sorted by key T cell subtype marker genes, *Foxp3*, *Cd4*, *Cd8a* and *Ctla4* (Figure S2A). Populations of cells were then defined using logical operators to include and exclude specific genes for specific cell types based on known flow cytometry gating strategies. For example, within the T_{het} cluster, $Cd8^+$ T cells were transcriptionally gated by the following criteria applied to the normalized count matrix: ((*Cd3d* >0 | *Cd3e* >0 | *Cd3g* >0) & (*Cd4* == 0) & (*Foxp3* == 0) & (*Cd8a* > 0 | *Cd8b1* >0) (Table S4). Applying the “OR” operator to genes with multiple subunits or chains (*Cd3*, *Cd8*) dramatically reduced the effect of drop-out with this gating approach. These individual T cell subtypes were then analyzed for treatment induced DEGs.

To construct expression heatmaps, relationships among genes were calculated across treatments as pairwise Pearson correlations. The resulting correlation matrix was converted to a dissimilarity matrix and clustered hierarchically by complete linkage clustering implemented by the R package hclust.

Analysis of ADT count data: batch correction

With the method of Cellular Indexing of Transcriptomes and Epitopes by Sequencing (CITE-seq), simultaneously measuring the mRNAs and a multitude of cell-surface proteins for single cells has become possible(Stoeckius et al., 2017). Sequencing antibody-derived tags (ADTs) allowed us to quantitatively study the surface protein expression on single cells. For each experiment sampling N cells, we constructed a matrix of ADT counts,

$$\begin{bmatrix} c_{1,1} & c_{1,2} & \cdots & c_{1,m} \\ c_{2,1} & c_{2,2} & \cdots & c_{2,m} \\ \vdots & \vdots & & \vdots \\ c_{N,1} & c_{N,2} & \cdots & c_{N,m} \end{bmatrix},$$

with $c_{i,j}$ denoting the count of the j-th antibody bound to the i-th cell. The sum s_i of the i-th row was the total number of ADTs measured from the i-th cell, and dividing each row by its row sum thus yielded a probability vector of antigens detected on the cell surface. In CITE-seq, as in other single-cell techniques, sequencing depths would differ from cell to cell, and this variation is partly reflected in the range of different s_i's. Moreover, some of the ADTs measured might come from nonspecific background binding, and calling true signals of antigen presence on a cell surface requires modeling the background distribution of ADT counts due to nonspecific binding. Similar to the published approach (Stoeckius et al., 2017), we used a low-level 'spike-in' control from another species to estimate this background distribution. More precisely, a small percentage (~5%) of human HEK293 cells was added to each sample of mouse skin cells. The ADT sequencing of spiked-in cells from our six samples showed some systematic differences that also persisted in the mouse cells. To remove these batch effects, we transformed the probability vectors of antigens described above by standardizing the ADT distributions of spiked-in cells across the six samples. Our standardization approach utilized differential geometry on the probability manifold of antigen frequencies as follows:

Taking data from the ADT assay, we represent a cell by a point on the $(m-1)$-dimensional simplex

$$\sum_{j=1}^{m} x_j = 1, \quad x_j \geq 0,$$

where x_j is the fraction of the j-th surface protein measured, calculated as $c_{i,j}/s_i$ for the i-th cell as previously described. The open probability simplex (i.e., the simplex minus its boundary), equipped with the coordinates (x_1, x_2, ..., x_m) and the Fisher-Rao metric $g_{jj'} = \delta_{jj'}/x_j$, forms a Riemannian manifold. It is well known (Amari and Nagaoka, 2007) that the open simplex can be isometrically mapped to the positive orthant of an $(m-1)$-dimensional hypersphere of radius 2 via the diffeomorphism

$$y_j = 2\sqrt{x_j}\,, \quad j = 1, \ldots, m,$$

where the metric on the hypersphere is induced by the Euclidean metric on the ambient flat space.

Principal component analysis (PCA) showed that the point clouds of spiked-in human cells were separated into batch clusters on the probability simplex, suggesting systematic differences in measurement among the samples. Similar patterns of batch effect were also observed for mouse cells. To standardize the data on probability simplex across samples, we first calculated the Riemannian mean (Riemannian center of mass) of the spiked-in human cells within each sample, using an iterative algorithm on the hypersphere (Åström et al., 2017). For each sample, we computed the geodesic path connecting its Riemannian mean to a fixed reference point and then "parallel transported" the point cloud of both human and mouse cells along the geodesic path towards the reference point. In our data, this reference point was computed as the Riemannian mean of pooled data from two samples of OXA-C and one sample of OXA that were most similar among the six samples. This standardization preserves the Fisher-Rao distance between cells and their respective Riemannian mean during the transport, thereby preserving the relative spatial distribution of point clouds on the probability simplex for each sample. Finally, we obtained the adjusted ADT counts by multiplying the standardized probabilities by the total number of ADT counts in each cell and rounding the products to integers.

Analysis of ADT count data: modeling nonspecific binding and calling signals

We modeled the background distribution of nonspecific ADTs using a zero-inflated negative binomial (ZINB) model for each surface protein separately, with the total ADT count s_i entering as the size factor for the i-th cell accounting for the differences in sequencing depths, and c_{ij} being the geodesic-corrected count number for the j-th surface protein:

$$\begin{aligned} P(c_{ij} \mid s_i, \pi_j, \alpha_j, \beta_j) &= \pi_j\, \delta[c_{ij}] + (1-\pi_j)\, \mathrm{NB}(c_{ij}\,;\, \mu_{ij} = s_i\, \alpha_j/\beta_j, \alpha_j) \\ &= \pi_j\, \delta\big[c_{ij}\big] + \big(1-\pi_j\big) \int_0^\infty \mathrm{d}\, \lambda_{ij}\; \Gamma\Big(\lambda_{ij}\,;\, \alpha_j, \beta_j\Big)\; \mathrm{Po}\big(c_{ij}\,;\, \lambda_{ij}\, s_i\big), \end{aligned}$$

where $\pi_j \in [0,1]$ is the parameter for zero inflation, and the pair (α_j, β_j) parameterizes the negative binomial (NB) component, which could be thought of as an infinite mixture of Poisson distributions Po with mean $\lambda_{ij}\, s_i$, with the mixing distribution being the Gamma distribution Γ parametrized by α_j and β_j (see, for example, (Zhou et al., 2012)).

We fitted these ZINB null models on the combined human spiked-in cells after batch correction, obtaining a set of parameters {π_j, α_j, β_j} for each antigen. For each mouse cell, we then calculated the p-value for every corrected ADT count using the ZINB null models. We used the Benjamini–Hochberg (BH) procedure to adjust for multiple hypothesis testing and computed the false discovery rate (FDR) (Benjamini and Hochberg, 1995) using the function p.adjust from the 'stats' package in R(R Core Team, 2013). We chose the FDR threshold of q=0.01 to call the presence of an antigen(Zhang et al., 2020).

Flow cytometry analysis

Flow cytometry analysis was performed on ear skin single cell suspensions from imiquimod or vanicream control treated mice. The single cell tissue suspension was stimulated ex vivo for 4 hours at 37℃ in DMEM supplemented with 10% FCS, 2 mM L-glutamine, 1 mm sodium pyruvate, 20 nM phorbol 12-myristate 13-acetate (PMA; Sigma), 1 uM ionomycin (Sigma) and 5 ug/ml brefeldin A (Sigma). For flow cytometry, cells were stained with eFluor-780 fixable viability dye (Invitrogen) and the following antibodies to cell surface antigens were used (anti-CD11b (1:200, M1/70, Biolegend), anti-CD11c (1:100, HL3, Thermofisher), anti-CD3epsilon (1:50, 145-2C11, Biolegend), anti-CD301b (1:25, URA-1, Biolegend), anti-CD4 (1:100, GK1.5, Biolegend), anti-CD45 (1:100, 30-F11, Biolegend), anti-CD8α (1:100, 53-6.7, Biolegend), anti-F4/80 (1:25, BM8, Biolegend), anti-γδTCR (1:100, GL3, Biolegend), and anti-I-A/I-E (1:100, M5/114, BD bioscience)), then fixed, permeabilized, and stained for intracellular antigens with anti-CCL5 (1:100, 2E9/CCL5, Biolegend), anti-IL-17A (1:50, eBio17B7, eBioscience), anti-IL-22 (1:100, Poly5164, Biolegend), and anti-Foxp3 (1:50, FJK-16s, eBioscience). Data were acquired on an LSRFortessa Flow Cytometer (BD) and analyzed using FlowJo 10.0 software (Tree Star).

Slingshot for trajectory and pseudotime

In order to assess for a common tissue migration trajectory in the mast/basophils cluster, we subsetted the mast/basophil cluster and utilized the Slingshot bioconductor package. After retaining robustly expressed genes with a minimum cluster size > 10 cells (geneFilter), we employed full quantile normalization followed by dimensionality reduction with PCA. After the

identification of clusters using *k*-means by $k = 2$ to avoid spurious branching events, we inferred the lineage with points colored by pseudotime. Genes associated with the course of development were applied to a general additive model to regress each gene on the pseudotime variable. The top 100 genes were chosen based on *p-val* and their expression over development was visualized via the plotheatmap function.

DiVNCE global transcriptional response analysis

The top 50 nearest neighbors to each treatment cell were calculated based on the Euclidean distance of the scaled and centered harmonized expression data generated by the integration procedure in Seurat (Stuart et al., 2019). If any control cell was found in this set of neighbors, the DiVNCE profile is the difference between the non-harmonized expression of 1,000 variable genes from the treatment cell and the nearest control cell. The 1,000 variable genes were selected based on dispersion of log-normalized counts per ten thousand across both the OXA and IMQ datasets. Expression values used to calculate the DiVNCE profiles are log-normalized counts per ten thousand that are then centered and scaled across all cells in both OXA and IMQ datasets. DiVNCE clusters were calculated separately for IMQ and OXA using the top 20 principal components of the DiVNCE profile data and the Louvain algorithm with resolution = 0.3. Adjusted rand index was calculated using the CrossClustering R package (Tellaroli et al., 2016).

Supplemental References

Amari, S., and Nagaoka, H. (2007). Methods of Information Geometry (American Mathematical Soc.).

Åström, F., Petra, S., Schmitzer, B., and Schnörr, C. (2017). Image Labeling by Assignment. J Math Imaging Vis *58*, 211–238.

Benjamini, Y., and Hochberg, Y. (1995). Controlling the False Discovery Rate: A Practical and Powerful Approach to Multiple Testing. Journal of the Royal Statistical Society: Series B (Methodological) *57*, 289–300.

Finak, G., McDavid, A., Yajima, M., Deng, J., Gersuk, V., Shalek, A.K., Slichter, C.K., Miller, H.W., McElrath, M.J., Prlic, M., et al. (2015). MAST: a flexible statistical framework for assessing transcriptional changes and characterizing heterogeneity in single-cell RNA sequencing data. Genome Biology *16*, 278.

Gray, E.E., Ramírez-Valle, F., Xu, Y., Wu, S., Wu, Z., Karjalainen, K.E., and Cyster, J.G. (2013). IL-17-committed Vγ4+ γδ T cell deficiency in a spontaneous Sox13 mutant CD45.1 congenic mouse substrain protects from dermatitis. Nat Immunol *14*, 584–592.

Luecken, M.D., and Theis, F.J. (2019). Current best practices in single-cell RNA-seq analysis: a tutorial. Molecular Systems Biology *15*, e8746.

Man, M.-Q., Hatano, Y., Lee, S.H., Man, M., Chang, S., Feingold, K.R., Leung, D.Y.M., Holleran, W., Uchida, Y., and Elias, P.M. (2008). Characterization of a Hapten-Induced, Murine Model with Multiple Features of Atopic Dermatitis: Structural, Immunologic, and Biochemical Changes following Single Versus Multiple Oxazolone Challenges. Journal of Investigative Dermatology *128*, 79–86.

R Core Team (2013). R: A language and environment for statistical computing. 1–16.

Stoeckius, M., Hafemeister, C., Stephenson, W., Houck-Loomis, B., Chattopadhyay, P.K., Swerdlow, H., Satija, R., and Smibert, P. (2017). Simultaneous epitope and transcriptome measurement in single cells. Nature Methods *14*, 865–868.

Stuart, T., Butler, A., Hoffman, P., Hafemeister, C., Papalexi, E., Mauck, W.M., Hao, Y., Stoeckius, M., Smibert, P., and Satija, R. (2019). Comprehensive Integration of Single-Cell Data. Cell *177*, 1888-1902.e21.

Tellaroli, P., Bazzi, M., Donato, M., Brazzale, A.R., and Drăghici, S. (2016). Cross-Clustering: A Partial Clustering Algorithm with Automatic Estimation of the Number of Clusters. PLOS ONE *11*, e0152333.

Zhang, S., Leistico, J.R., Cook, C., Liu, Y., Cho, R.J., Cheng, J.B., and Song, J.S. (2020). Riemannian geometry and statistical modeling correct for batch effects and control false discoveries in single-cell surface protein count data. Phys. Rev. E *102*, 012409.

Zhou, M., Hannah, L., Dunson, D., and Carin, L. (2012). Beta-Negative Binomial Process and Poisson Factor Analysis. ArXiv:1112.3605 [Stat].